



Università di Pisa

MATHEMATICAL, PHYSICAL AND NATURAL SCIENCES AREA
Department of Physics

MASTER DEGREE THESIS

**Design of a delay mask for pulse train generation
in laser wakefield acceleration experiments**

CANDIDATE

Gianluca Vantaggiato

SUPERVISOR

Leonida A. Gizzi

CO-SUPERVISOR

Luca Labate

A mia madre

RINGRAZIAMENTI

Non faccio uno sgrabo a Umberto Eco, contrario al ringraziare i relatori, perché il dott. Gizzi e il dott. Labate, Leo e Luca, non hanno semplicemente ottemperato ai loro doveri ma mi hanno accompagnato e supportato, mi hanno consigliato e mostrato e di questa spontanea eccedenza li ringrazio.

Ci si conosceva già, evidentemente non abbastanza. Poi sulle spallette (l'uno dell'altro/a) ci hanno unito i silenzi, Matteo, e le parole, Antronella. Quello che siete me lo porto dentro ma so che questa pagina verrà letta oggi o tra molti anni, e oggi e tra molti anni si deve sapere che grazie a voi è stato bello il giusto, così *bu pigghiu pe fessa*.

Ringrazio i luoghi, la caserma, la casadeisiciliani, cavalieri, lungarni, aulestudio, vicoli, Pisa, perché sono stati abitati anche da Rosa, Damiano, Christian, Tommaso, Valeria, Guarino, Alice e da tanti ospiti e da ancora più storie, la nostra universitaria epica personale, sopravvalutata e indimenticabile.

Su panchine infinite di chiacchiere e tempi sospesi, le cose che succedono sempre altrove, lì, raccontandocene, si realizzano; grazie per aver sempre trovato il tempo di sederci, Rob. D'altronde ci è bastato passeggiare una volta per farmi passare dalle inerzie alle scelte, con l'intercessione di Giulia, sempre sia ringraziata.

Per il cambiamento inatteso, le bicicletate, la procrastinazione, la motivazione, le sere, gli sproni, i concerti, lo scalpitare, gli animali, le acque, le paure, le conferme, le risate, il mangiare, i dubbi, la neve, il viaggiare, l'irrequietezza, il leggere, il non elencato, il tutto, grazie Serena di essere stata; passato perennemente prossimo.

Grazie famiglia tutta, di aver concesso, accettato, provveduto e aiutato, di essere casa, ché Uccia è più della somma dei nipoti.

Pisa, 17 ottobre 2019.

Gianluca Vantaggiato

CONTENTS

ACKNOWLEDGEMENTS	v
INTRODUCTION	ix
1 LASER-PLASMA ACCELERATION	1
1.1 Electromagnetic waves	1
1.1.1 Gaussian beams	3
1.1.2 Pulse optics	5
1.1.3 Pulse propagation	9
1.2 High-power lasers	13
1.2.1 Laser systems evolution	13
1.3 Introduction to plasmas	16
1.4 Laser-plasma acceleration	18
1.4.1 LWFA	18
2 THE E.M. FIELD IN THE FOCAL REGION OF AN OAP	21
2.1 Geometrical and theoretical framework	22
2.1.1 Overview	22
2.1.2 Off-Axis Parabolic mirror	24
2.1.3 Reflected electromagnetic fields	27
2.1.4 Full vector diffraction model for an OAP	28
2.2 Numerical integration	32
2.3 Intra-cycle depolarization	35
2.3.1 Overview	36

2.3.2	Simulations	37
2.3.3	Parametric dependence of the depolarization	42
3	A SIMPLE METHOD FOR PULSE TRAIN GENERATION	47
3.1	The idea	48
3.1.1	Pulse train generation	48
3.1.2	The delay mask	52
3.2	Spatial characterization	52
3.2.1	Early designs	54
3.2.2	Final design	58
3.3	Temporal characterization	60
	CONCLUSIONS	67
	ACRONYMS	69
	BIBLIOGRAPHY	71

INTRODUCTION

Since their first appearance in 1960, lasers have boosted up studies in many areas due to the high fields provided, opening the possibility to investigate a wide range of phenomena. During these years there have been huge improvements in laser pulse generation, most notably the recent Nobel prize-winning amplification technique of Chirped Pulse Amplification (CPA), leading to nowadays systems capable of pulse duration of the order of few femtoseconds and with peak intensity, when focused, exceeding 10^{20} W/cm² thus concerning the ultra-relativistic regime.

In 1979 Tajima and Dawson [1] proposed the use of a single high-intensity ultrashort laser pulse to excite longitudinal waves in plasmas via the ponderomotive force. Such waves, exploited as accelerating structure, can sustain fields of the order of 100 GV/m, way more than conventional accelerators and without the breakdown constraint. This model, namely Laser WakeField Acceleration (LWFA), has proven his validity, already reaching accelerated electron beam energy up to 8 GeV [2]. However the poor quality of these accelerated bunches limits the applications of laser-plasma accelerators. One of the proposed solution is to decouple the wakefield generation and the injection mechanism.

Among the proposed models, the REsonant Multi-Pulse Ionization injection (REMPI) scheme [3] aims to obtain electron bunches with low emittance (0.08 mm mrad) and low energy spread (0.65 %). In this model the wake is excited by a train of resonant low-energy pulses generated from a single high-energy ultrashort pulse. Part of the original pulse is doubled

in frequency and grants the ionization injection.

In my thesis I focused on the design process, from the development of an original theoretical model to a possible experimental implementation, of a simple method of generating the pulse train from a single high-energy pulse. Particular attention has been devoted to the development of a cost-effective system that could be easily integrated in existing LWFA experiments. The choice landed on a delay mask, an optical component consisting of a disk divided in rings of different thicknesses, placed right before the last focusing optic, typically an Off-Axis Parabola (OAP). In this way the transverse profile of the original single pulse is split in different sections, delayed accordingly to the plasma period, that, once focused, result in a train of pulses at the focal plane of the OAP, where the target is usually placed.

In the first chapter the physical context is presented, i.e. the basics of laser beam and pulse characterization together with a brief introduction to the laser-plasma acceleration field. The second chapter is devoted to the development of the theoretical and geometrical model for numerical computation of the electromagnetic fields of a laser beam focused by an OAP. As evidence of the model validity, a remarkable application is also presented, describing an intra-cycle depolarization [4], due to the focusing by an OAP, of an initially linearly polarized laser beam. Finally, the focus of the third chapter is entirely on the delay mask, from the preliminary designs to the final characterization of the spatial and temporal profiles of the pulse train, investigating the viability of such an approach for modern laboratories.

LASER-PLASMA ACCELERATION

The interaction between a ultra-short, high intensity laser pulse and a plasma can excite longitudinal electrostatic waves, capable of sustaining fields of the order of 100 GV/m and beyond. Such waves can be used to accelerate charged particles to GeV energy in a few centimeters, in comparison to the several kilometres of the traditional radio-frequency accelerators and without the limitation given by the material breakdown, as plasma is already ionized. Due to these features, a great interest is being devoted to this technology, boosted in the last decades by the development of compact table-top terawatt laser systems.

In this chapter a brief introduction on laser systems is presented together with the description of the ultra-short laser pulse propagation properties relevant for the modelling proposed in the second and third chapter. The theoretical background of laser-plasma interaction is also introduced in order to specify the physical framework of these experiments and clarify some concepts.

1.1 ELECTROMAGNETIC WAVES

The description of the radiation emitted by laser systems is described by classical electrodynamics. The electromagnetic field is represented by

two vector quantities, the electric field $\mathbf{E}(\mathbf{r}, t)$ and the magnetic one $\mathbf{B}(\mathbf{r}, t)$. These vectors are finite and continuous functions of the position \mathbf{r} in space and time t . The general description of electromagnetic phenomena is provided by the set of Maxwell's equations. In vector formalism and using standard SI units they are formulated as follows [5]

$$\nabla \cdot \mathbf{E} = \frac{\rho}{\epsilon_0} \quad (1.1)$$

$$\nabla \cdot \mathbf{B} = 0 \quad (1.2)$$

$$\nabla \times \mathbf{E} = -\frac{\partial \mathbf{B}}{\partial t} \quad (1.3)$$

$$\nabla \times \mathbf{B} = \mu_0 \left(\mathbf{J} + \epsilon_0 \frac{\partial \mathbf{E}}{\partial t} \right), \quad (1.4)$$

where $\rho(\mathbf{r}, t)$ is the total electric charge density and $\mathbf{J}(\mathbf{r}, t)$ is total electric current density due to the motion of charged particles. These quantities may be continuous as well as discrete. The universal constants appearing in the equations are the electric permittivity of vacuum ϵ_0 and the magnetic permeability of vacuum μ_0 . As shown by Maxwell's equations, the charge density is the source of the electric field, whilst the magnetic field is produced by the current density.

In the absence of external sources though, it might be shown that eqs. (1.1) to (1.4) may be alternatively formulated as uncoupled homogeneous wave equations for electric field $\mathbf{E}(\mathbf{r}, t)$ and magnetic field $\mathbf{B}(\mathbf{r}, t)$ in order to retrieve an analytical formulation of the electromagnetic waves. The wave equations are

$$\Delta \mathbf{E} - \frac{1}{c^2} \frac{\partial^2 \mathbf{E}}{\partial t^2} = 0 \quad (1.5)$$

$$\Delta \mathbf{B} - \frac{1}{c^2} \frac{\partial^2 \mathbf{B}}{\partial t^2} = 0, \quad (1.6)$$

where the universal constant

$$c = 1/\sqrt{\mu_0 \epsilon_0} \quad (1.7)$$

is the speed of light in vacuum, which leads to the essential fact that the electromagnetic waves propagate in vacuum with the velocity of light. However, the wave eqs. (1.5) and (1.6) do not provide all the information about the electric and magnetic field of the wave. There are further constraints due to the Maxwell's equations restricting the orientation and proportional magnitudes of the fields. From eqs. (1.1) to (1.4) it might be clearly seen that $\mathbf{E}(\mathbf{r}, t)$ and $\mathbf{B}(\mathbf{r}, t)$ must be mutually perpendicular to each other as well as to the direction of the wave propagation [6].

1.1.1 GAUSSIAN BEAMS

Without any loss of generality, we consider the laser beam as a monochromatic electromagnetic wave propagating toward the positive direction of the z -axis. The description of such a wave is given by the evolution of a single electric field component linearly polarized along the x -axis of the Cartesian coordinate system, therefore one has to look for the solution of eq. (1.5).

According to the previous assumptions, the solution is expected to be in the form of the plane wave

$$\mathbf{E}(\mathbf{r}_\perp, z, t) = \text{Re}\left(E_0 \Psi(\mathbf{r}_\perp, z) e^{i(k_z z - \omega t)}\right) \hat{\mathbf{x}}, \quad (1.8)$$

where $\mathbf{r}_\perp = \mathbf{x} + \mathbf{y}$ is the vector of transverse Cartesian coordinates, symbol Re stands for the real part of the complex quantity, E_0 is a constant amplitude, $\Psi(\mathbf{r}_\perp, z)$ is the part of the wave function which is dependent only on the spatial coordinates, ω denotes the angular frequency and k_z is the z -component of the wave vector \mathbf{k} . Direct substitution of eq. (1.8) into eq. (1.5) yields the time-independent form of the scalar wave equation

$$\Delta \Psi(\mathbf{r}_\perp, z) + 2ik_z \frac{\partial \Psi(\mathbf{r}_\perp, z)}{\partial z} = 0, \quad (1.9)$$

also known as the paraxial Helmholtz equation [7], the starting point of the traditional Gaussian beam theory. This approximation allows the omission of the term with the second-order derivative in the propagation equation

(as derived from Maxwell's equations), so that a first-order differential equation results. The solution can be thus expected to be in the form of a Gaussian function, and after some algebra, one can write

$$\Psi(\mathbf{r}_\perp, z) = \frac{w_0}{w(z)} \exp \left[-\frac{\mathbf{r}_\perp^2}{w(z)^2} + i \left(k_z \frac{\mathbf{r}_\perp^2}{2R(z)} - \varphi_G(z) \right) \right], \quad (1.10)$$

where the parameters are defined as

$$w(z) = w_0 \sqrt{1 + \left(\frac{z}{z_R} \right)^2}, \quad R(z) = z \left[1 + \left(\frac{z_R}{z} \right)^2 \right], \quad \varphi_G(z) = \arctan \left(\frac{z}{z_R} \right). \quad (1.11)$$

Before describing these three quantities it is necessary to explain what parameters they depend on. w_0 is the beam waist, defined as the radius at which the laser intensity fall to $1/e^2$ of its axial value at the focal spot. The second parameter, $z_R = \frac{\pi w_0^2}{\lambda}$, is the Rayleigh length which is the distance in the longitudinal direction from the focal spot to the point where the beam radius is $\sqrt{2}$ larger than the beam waist w_0 . There is also another useful parameter to mention: it is denoted by $\Theta = \frac{\lambda}{\pi w_0}$ and it is the divergence angle of the beam that represents the ratio of the transverse to the longitudinal extent. Note that these parameters are exploited in the geometry description of focused beams.

Back to the Gaussian beam parameters, the function $w(z)$ represents the spot size parameter of the beam, that is the radius at which the laser intensity fall to $1/e^2$ of its axial value at any position z along the beam propagation. Note that the beam waist correspond to the minimum spot size ($w(0) = w_0$). $R(z)$, is the radius of curvature of the beam wavefront at any position z along the beam propagation axis. Note that $\lim_{z \rightarrow 0} R(z) = \infty$, i.e. the beam behaves like a plane wave at focus as required. Finally, $\varphi_G(z)$, known as Gouy phase, describes a phase shift in the wave as it passes through the focal spot.

1.1.2 PULSE OPTICS

Lasers are characterized by a variety of parameters, but a core distinction can be made, based on the produced radiation, between lasers operating in Continuous-Wave (CW) and pulsed mode. As the name suggests CW lasers are generally characterized by the constant emission of monochromatic light, thus having a constant output power over time. For example, among modern technology, fiber lasers are able to reach tens of kW of CW optical power [8].

However, in order to reach very high power, a *pulsed* mode is used in which energy is concentrated in a short time. In this way pulsed lasers have higher peak power for the same average energy per unit time with respect to CW lasers. Intuitively the peak power P_p increases inversely with the pulse duration Δt (intended as the Full Width at Half Maximum (FWHM)), which can be written [9]

$$P_p = k_s \frac{\mathcal{E}_p}{\Delta t}, \quad (1.12)$$

where \mathcal{E}_p is the laser energy and k_s is a constant that depends upon the pulse shape¹.

From the previous equation one could think to shrink the pulse duration as much as desired but that is not possible due to the dependence between duration and spectral width.

Consider a generic monochromatic plane wave with the transverse electric field given by

$$E_y = \text{Re}(E_0 e^{i\omega_0 t}), \quad (1.13)$$

where ω_0 is the angular frequency. Such wave extends indefinitely in time and space, i.e. its duration is infinite, and, by definition, its spectrum consists only of the oscillating frequency ω_0 .

The thorough mathematical approach makes use of the Fourier transform to switch between the time domain and the frequency domain of a

¹For a Gaussian pulse shape $k_s = 0.94$

wave, written as [10]

$$E(\omega) = \int_{-\infty}^{+\infty} E(t)e^{-i\omega t} dt \equiv \mathcal{F}\{E(t)\} \quad (1.14)$$

for the direct Fourier transform and

$$E(t) = \frac{1}{2\pi} \int_{-\infty}^{+\infty} E(\omega)e^{i\omega t} d\omega \equiv \mathcal{F}^{-1}\{E(\omega)\} \quad (1.15)$$

for the inverse one.

Applying the transform to the plane wave one gets

$$E(\omega) = \int_{-\infty}^{+\infty} e^{i(\omega-\omega_0)t} dt = \delta(\omega - \omega_0), \quad (1.16)$$

$\delta(\omega - \omega_0)$ being the Dirac distribution centered in ω_0 with a zero width, thus confirming the presence a singular frequency. Note that this is true for a wave propagating throughout an infinite amount of time. Just the assumption that a wave vanishes at a certain far-away moment results in a broadening of the Dirac distribution, hence the appearing of a frequency spectrum.

On the other hand a pulsed wave, or pulse, has, by definition, a finite duration, so, in order to study its spectrum, consider the same wave of eq. (1.13) and multiply it by a Gaussian envelope (see FIG. 1.1(A))

$$E_y = \text{Re}\left(E_0 e^{-\Gamma t^2 + i\omega_0 t}\right), \quad \Gamma \in \mathbb{R}^+, \quad (1.17)$$

where Γ is the real-valued shape factor of the envelope, proportional to the inverse of the squared pulse duration. This time the Fourier transform yields

$$E(\omega) = \exp\left(\frac{-(\omega - \omega_0)^2}{4\Gamma}\right), \quad (1.18)$$

which is still a Gaussian function, centered in ω_0 , with a finite spectrum width proportional to Γ . Hence the result of applying an envelope to a monochromatic wave is the appearance of a frequency spectrum in spite of the unique central one. Pulses can be in general defined by different bell-shaped functions, i.e. functions that asymptotically vanish for

large positive and negative abscissa and with a single maximum, but the Gaussian function being its own Fourier transform makes it particularly convenient.

The relation between pulse duration and spectrum width can be inferred from their statistical definitions

$$\langle \Delta t \rangle = \frac{\int_{-\infty}^{+\infty} t |E(t)|^2 dt}{\int_{-\infty}^{+\infty} |E(t)|^2 dt}, \quad (1.19)$$

$$\langle \Delta \omega \rangle = \frac{\int_{-\infty}^{+\infty} \omega^2 |E(\omega)|^2 d\omega}{\int_{-\infty}^{+\infty} |E(\omega)|^2 d\omega}, \quad (1.20)$$

which can be shown to be [10]

$$\Delta t \Delta \omega \geq \frac{1}{2}. \quad (1.21)$$

This classical-physics relation, reminiscent of the quantum-mechanical time-energy uncertainty principle, can be expressed in terms of more suitable quantities from an experimental point of view, such as

$$\Delta \nu \Delta t = K, \quad (1.22)$$

where $\Delta \nu$ is the frequency FWHM, as well as Δt is the FWHM pulse duration and K is a constant which value depends upon the shape of the pulse. Recalling that $|\Delta \nu / \nu_0| = \Delta \lambda / \lambda_0$ (ν_0 being the central frequency and λ_0 the corresponding wavelength) and that $c = \lambda \nu$, c being the velocity of light, it is possible to write the previous equation in terms of the wavelength bandwidth $\Delta \lambda$

$$\Delta t = K \frac{\lambda_0^2}{c \Delta \lambda}. \quad (1.23)$$

This relationship has several consequences on ultra-short light pulses. Mainly it means that the generation of a light pulse with a given duration is constrained by the use of a broad enough spectral bandwidth. For example, a Gaussian-shaped pulse ($K = 0.441$) with a central wavelength of 800 nm and a duration of 40 fs has a wavelength extension of 23.5 nm. Gaussian

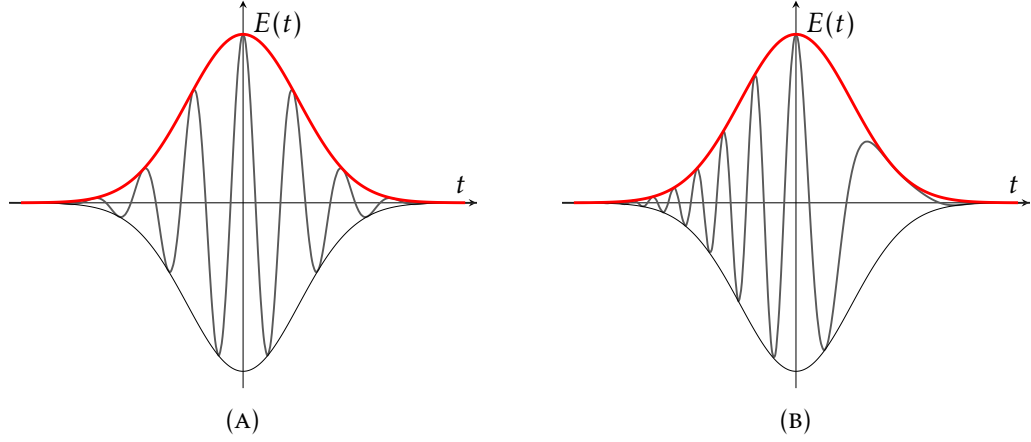


FIGURE 1.1: Time evolution of a pulse. (A) represents a simple pulse built by multiplying a cosine function (in grey) by a Gaussian-shape envelope (in red). (B) represents the same pulse with the introduction of a negative *chirp*, i.e. a quadratic dependence upon time resulting in the frequency linearly diminishing through its evolution.

functions have also the property of being the most “efficient” envelope since the equality in eq. (1.21) is reached only using such profile. In this case the pulse is called Fourier-transform-limited and has the shortest possible duration.

As a final remark on pulse description, let’s focus on the instantaneous frequency. Considering again the light pulse as in eq. (1.13), the instantaneous frequency is obtained as the time derivative of the phase, readily

$$\omega(t) = \frac{d\Phi}{dt} = \omega_0. \quad (1.24)$$

As expected the angular frequency is constant and equals the central wavelength ω_0 and the pulse, as already seen, is transform-limited. Introduce now an arbitrary quadratic dependence upon time in the phase of the pulse, as in

$$E_y = \text{Re}\left(E_0 e^{-\Gamma t^2 + i(\omega_0 t + \alpha t^2)}\right), \quad \alpha \in \mathbb{R}. \quad (1.25)$$

Calculating again the instantaneous frequency one gets

$$\omega(t) = \frac{d\Phi}{dt} = \omega_0 + \alpha t, \quad (1.26)$$

which readily means that the frequency varies linearly² in time. A pulse exhibiting this behaviour is called *chirp*³. More specifically, when the frequency increases ($\alpha > 0$) it is called *up-chirped* pulse whilst *down-chirped* when the frequency decrease ($\alpha < 0$). A graphical example of the latter is displayed in FIG. 1.1(B). The role of this characteristic will be clarified in the following discussion on pulse propagation.

1.1.3 PULSE PROPAGATION

When considering the propagation of ultra-short pulses in optical media dispersion phenomena become important. The velocity of propagation of an electromagnetic wave is frequency dependent, except in vacuum, where all electromagnetic waves travel at the same phase velocity (the speed of light), as can be demonstrated through solving Maxwell's equations [5].

The physical origin of dispersion can be accounted for by considering the propagation of an electromagnetic wave through an atomic or molecular medium. This propagation occurs due to the atoms becoming polarized by the passing oscillatory electromagnetic field and, provided there is no absorption, the wave propagates through the medium undisturbed thanks to the quasi-elastic restoring force acting on the electrons that have been polarized within the atomic or molecular medium. However at frequencies where there is absorption, energy is transferred from the wave into the medium, with the energy dissipated either in the form of subsequent atomic emissions or heat. The polarizability of a medium therefore defines the propagation of electromagnetic waves which pass through the medium, and

²The number 2 at the denominator has been embedded in α for readability and without losing generality.

³The word is a reference to birds' chirp, the pitch of which changes from the start to the end of the sound.

features complex behaviours such as resonances around given frequencies. This polarizability is therefore a complex function which depends upon the exact response of the atoms or molecules to a propagating electromagnetic wave.

The polynomial expansion of the macroscopic polarization induced by an electric field \mathbf{E} clearly shows the different regimes of study. It is given by

$$\frac{\mathbf{P}}{\epsilon_0} = \chi^{(1)} \cdot \mathbf{E} + \chi^{(2)} \cdot \mathbf{E}\mathbf{E} + \chi^{(3)} \cdot \mathbf{E}\mathbf{E}\mathbf{E} + \dots \quad (1.27)$$

where ϵ_0 is the electric permittivity. The linear first-order term in the electric field describes the so called linear optics, while the nonlinear higher-order terms account for nonlinear optical effects.

In order to write the analytical expressions of the dispersion parameters in the linear optics regime, consider again a generic Gaussian pulse with the transverse electric field given by

$$E_y = \text{Re}\left(E_0 e^{-\Gamma t^2 + i\omega_0 t}\right), \quad (1.28)$$

and the Fourier transform of which has already been written as

$$E(\omega) = \exp\left(\frac{-(\omega - \omega_0)^2}{4\Gamma}\right). \quad (1.29)$$

Considering now that the pulse propagates inside a medium in the x direction, the spectrum becomes

$$E(\omega, x) = E_0(\omega) e^{-ik(\omega)x}, \quad (1.30)$$

where $k(\omega)$ is the frequency-dependent wave number, namely

$$k(\omega) = n(\omega) \frac{\omega}{c}. \quad (1.31)$$

n is the refractive index of the medium and it is also frequency-dependent. Assuming that the bandwidth $\Delta\omega \ll \omega_0$ (condition only weakly true for ultra-short pulses) one can express k in terms of the angular frequency ω applying a Taylor expansion:

$$k(\omega) = k(\omega_0) + k'(\omega - \omega_0) + k''(\omega - \omega_0)^2 + \mathcal{O}(\omega^3), \quad (1.32)$$

where

$$k' = \left(\frac{dk}{d\omega} \right)_{\omega_0} \quad k'' = \left(\frac{d^2k}{d\omega^2} \right)_{\omega_0}. \quad (1.33)$$

Therefore substituting in eq. (1.30) the spectrum becomes

$$E(\omega, x) = \exp \left[-ik(\omega_0)x - ik'x(\omega - \omega_0) - \left(\frac{1}{4\Gamma} + \frac{i}{2}k''x \right) (\omega - \omega_0)^2 \right] \quad (1.34)$$

from which one can retrieve the time evolution of the electric field operating the inverse Fourier transform (1.15) so that

$$E(t, x) = \sqrt{\frac{\Gamma(x)}{\pi}} \exp \left[i\omega_0 \left(t - \frac{x}{v_\phi(\omega_0)} \right) \right] \times \exp \left[-\Gamma(x) \left(t - \frac{x}{v_g(\omega_0)} \right)^2 \right], \quad (1.35)$$

where

$$v_\phi(\omega_0) = \left(\frac{\omega}{k} \right)_{\omega_0} \quad v_g(\omega_0) = \left(\frac{d\omega}{dk} \right)_{\omega_0} \quad \frac{1}{\Gamma(x)} = \frac{1}{\Gamma} + 2ik''x, \quad (1.36)$$

with the definition of v_ϕ and v_g being the phase velocity and the group velocity, respectively, while the term k'' is called Group Velocity Dispersion (GVD). Recalling the expressions for the wave number k and the wavelength λ in a medium

$$k = \frac{2\pi}{\lambda} \quad \lambda = \frac{2\pi c}{\omega n(\omega)} \quad \Rightarrow \quad k = \frac{\omega n(\omega)}{c}, \quad (1.37)$$

it is possible to write the velocities in terms of n as

$$v_\phi = \frac{c}{n} \quad (1.38)$$

$$v_g = \frac{1}{dk/d\omega} = \frac{c}{n} \frac{1}{1 + \frac{\omega}{n} \frac{dn}{d\omega}} = \frac{c}{n} \frac{1}{1 - \frac{\lambda}{n} \frac{dn}{d\lambda}}. \quad (1.39)$$

The first exponential term of eq. (1.35) expresses a delay of the central wavelength ω_0 by an amount x/v_ϕ . Because of the nature of the phase, not being a measurable quantity, this effect has no observable consequences. The second term, instead, contains two important information: the pulse keeps a Gaussian envelope and its maximum is delayed by an amount x/v_g .

In order to characterize the evolution of the Gaussian envelope, one can rewrite $\Gamma(x)$ as

$$\Gamma(x) = \frac{\Gamma}{1 + \xi^2 x^2} - i \frac{\Gamma}{1 + \xi^2 x^2}, \quad \xi = 2\Gamma k'', \quad (1.40)$$

and substitute in the second exponential term of eq. (1.35). It yields

$$\exp \left[-\frac{\Gamma}{1 + \xi^2 x^2} \left(t - \frac{x}{v_g} \right)^2 + i \frac{\Gamma \xi x}{1 + \xi^2 x^2} \left(t - \frac{x}{v_g} \right)^2 \right]. \quad (1.41)$$

The real part represents the delayed Gaussian function with a shape factor

$$\frac{\Gamma}{1 + \xi^2 x^2} \quad (1.42)$$

always smaller than the original one, which means that the pulse faces a broadening in duration as the effect of GVD. The imaginary part adds a quadratic time term to the phase, introducing, as already seen, a linear chirp in a previously transform-limited pulse. On the other side this also means that an initially chirped pulse that propagates through a medium can overcome this effect and even shrink its duration, based on chirp value.

In summary, this discussion on linear optics shows the importance of dispersion effects on a propagating pulses, which, even limiting the expansion to the second term, undergo a group delay, a duration increase and a chirp.

Third Order Dispersion (TOD) and Fourth Order Dispersion (FOD) can be evaluated as well, considering higher term of the Taylor series eq. (1.32). Since they are not needed for the purpose of this thesis, only a brief description of their effect will be given.

TOD results in a set of sub pulses that follows or precedes, based on the sign, the main pulse.

FOD induces, as the GVD, a symmetrical stretch in time domain with a more complex shape.

1.2 HIGH-POWER LASERS

Lasers are among the most significant inventions of the last century. Since their first appearance in 1960 [11], they boosted up the studies in many fields and provided an excellent source of high fields thus opening the opportunity to understand and investigate a wide range of phenomena, such as the atomic behaviour of matter or to observe nonlinear effects.

1.2.1 LASER SYSTEMS EVOLUTION

In the early years, the evolution of laser intensity was marked by two main innovations: first *Q-switching* [12] and later *mode-locking* [13]. The former is based on increasing the number of electrons in the excited state of the laser active medium by mean of a sudden variation of the quality factor of the resonator cavity. The latter instead exploits the phase coherence of the cavity modes in the resonator. Both schemes result in a *pulsed* emission.

In order to reach high intensities, the laser emission of the resonator cavity can be fed into a sequence of amplifying stages; before 1985 all amplifier systems were based on direct amplification. Indeed, if coherent radiation is made to pass through an excited active medium, it stimulates further coherent radiation emission. Thus a laser pulse can be coherently amplified extracting energy from the active medium. A good amplification efficiency is reached when the initial fluence of the pulse is of the order of the saturation fluence of the material, i.e. the maximum energy per unit area that can be extracted from the amplifier. This value, given by $F_{\text{sat}} = \frac{\hbar\omega}{\sigma}$, where \hbar is Planck's constant, ω the angular laser frequency and σ the amplifying transition cross section of the material, is of the order of J/cm^2 for crystals and mJ/cm^2 for dyes and excimers. The initial approach was to use the latter ones, materials with low-energy storage, and to increase the laser beams width in order to lower laser intensity thus preventing nonlinear effects and the "breakdown" of the optical components, i.e. the ionization of the materials involved in the beam line.

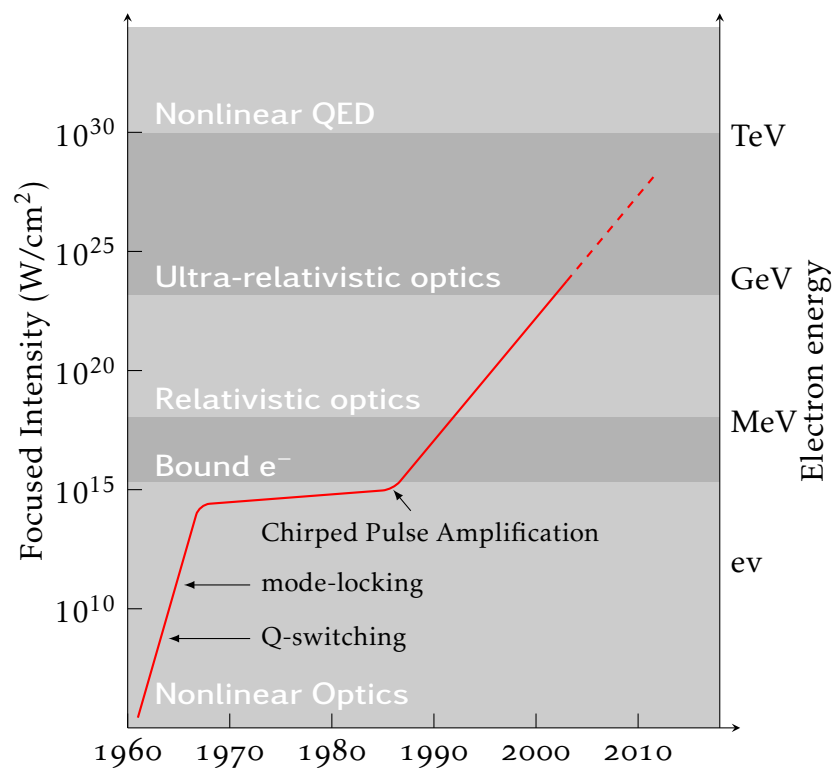


FIGURE 1.2: Historical evolution of lasers intensity. Picture adapted from [14].

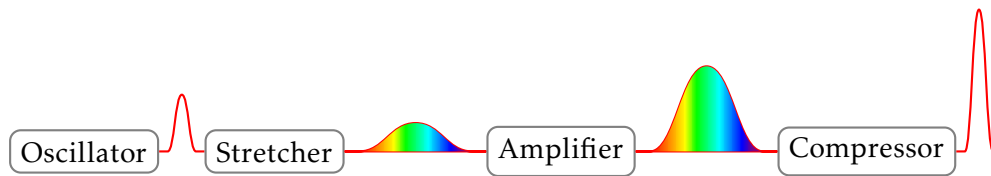


FIGURE 1.3: Schematic stages of CPA.

Moreover, the pulsed nature of these lasers sets a strong limit to the amplification process since the pulse duration is related to its spectral width such that short pulses contain wide frequency components (see eq. (1.23)). This means that for shorter pulses it would be necessary to have active mediums with larger gain bandwidth.

As a consequence of these limitations, the maximum focused intensity reached through the years remained almost the same for over a decade (see FIG. 1.2), until the introduction of the Chirped Pulse Amplification (CPA) [15].

This technique, awarded with Nobel Prize in physics in 2018, consists essentially in manipulating the pulse in order to simplify the amplification processes. The temporal duration of the laser pulse is increased introducing a chirp: by means of a couple of gratings the spectral components of the pulse are dispersed according to their frequency. This *stretched* pulse is easier to amplify efficiently, lowering the risks of damage for the optical components. After the amplification stage, the dispersion of spectral components can be reversed in the compressor stage with another couple of gratings, bringing the pulse duration back to close to its initial value. FIG. 1.3 shows a conceptual representation of the CPA steps. Most of the high-power laser systems employ this method, reaching focused intensity up to $10^{20} \text{ W cm}^{-2}$.

1.3 INTRODUCTION TO PLASMAS

The general definition of plasma is a collection of ionized matter that admits quasi-neutrality and exhibits collective behaviour [16]. The term quasi-neutrality means neutral enough so that the electron and ion charge densities are approximately equal over a large scale. Collective behaviour implies the existence of long ranged electromagnetic force; then the motion depends not only on local conditions, but on remote regions of plasma as well.

However, on the timescale of an ultra-short laser pulse, only the motion of electrons needs to be considered as the ions have much larger masses, and they can thus be treated as a stationary, positively charged background. The motion of an electron in external electric and magnetic fields is described by the Lorentz equation, and when the time duration of the laser pulse is very short, the result is a time-averaged force called the ponderomotive force, \mathbf{f}_p . It is showed to be [17]

$$\mathbf{f}_p \propto -\frac{q^2}{m} \nabla I, \quad (1.43)$$

where q and m are the particle charge and mass, respectively. This means that charged particles are pushed away from regions of high intensity irrespective of the sign of q , and the force is greater for the lightest particles, i.e. electrons. The resulting charge separation creates electrostatic fields, and displaced electrons behind the laser pulse will start to oscillate. Globally, a plasma has no net charge, so $n_e = Z n_i$, where n_i is the ion number density. The local charge displacement introduced by the laser pulse is shielded by plasma electrons over a characteristic distance called the Debye length, defined as

$$\lambda_D = \sqrt{\frac{\epsilon_0 k_B T_e}{q_e^2 n_e}}, \quad (1.44)$$

where ϵ_0 is the permittivity in free space, k_B the Boltzmann's constant and T_e is electron temperature. Physically, the Debye length decreases

with increasing electron number density, since more electrons are available for shielding. It is also reasonable that λ_D increases with T_e , since the electrons become more spread out at higher temperatures. The plasma response to an external electric field is not instantaneous but depends on its characteristic time scale. Introducing the plasma frequency as

$$\omega_{pe} = \sqrt{\frac{q_e^2 n_e}{\epsilon_0 m_e}}, \quad (1.45)$$

the plasma response to external perturbation can be seen as ω_{pe}^{-1} .

It is also possible to derive a wave equation that describes the collective motion of electrons in plasmas. For small charge density displacements Δn_e its solution yields a dispersion relation for the propagation of an electromagnetic wave with frequency ω_0 in the plasma

$$\omega_0^2 - \omega_{pe}^2 = k^2 c^2. \quad (1.46)$$

From the previous equation it is possible to define two different types of plasmas. The first is $\omega_0 < \omega_{pe}$, for which k becomes imaginary. In this case, the plasma is called *overdense*, and the electrons are able to move together with the electric field in the laser pulse, which means that the laser field is effectively stopped and the pulse cannot propagate through the plasma. The second case is when $\omega_0 > \omega_{pe}$, and the plasma is transparent to the incoming laser pulse. This is called an *underdense* plasma, and arises from low-density targets, such as gases and plasmas expanding into vacuum. It is possible to determine a critical density n_c at which the laser frequency is equal to the plasma frequency, which defines the boundary between these two regimes

$$n_c = \frac{\epsilon_0 m_e \omega_0^2}{q_e^2}. \quad (1.47)$$

Overdense plasmas are often formed when an intense laser pulse interacts with a solid target. This type of plasma can be used for ion acceleration, typically in Target Normal Sheath Acceleration (TNSA). However a brief discussion of different acceleration is provided in what follows.

1.4 LASER-PLASMA ACCELERATION

One of the most important application of laser-plasma interaction is the acceleration of charged particles. Nowadays, traditional radio-frequency accelerators are the prevalent and most reliable source of accelerated particle but this technology has some limitations, mainly due to the material breakdown of the components. Plasmas don't have such a constraint, being already ionized, and are capable of sustaining field of the order of hundreds of GV/m.

Hence the recent years have been particularly exciting for this field of study and several models have been proposed for different acceleration scheme. There is one aspect, though, in common for every setups: in order to obtained the necessary high intensity onto the target, the laser pulse need to be focused. And the higher the pulse energy becomes the more precise the focused electromagnetic fields characterization needs to be.

As a reference case a brief discussion on electron acceleration is presented.

1.4.1 LWFA

In 1979 TAJIMA and DAWSON [1] proposed the use of a short laser pulse of a very high intensity, to excite a longitudinal wakefield in the plasma. This model is called Laser WakeField Acceleration. When such a high intensity laser pulse is incident on a gas target, its leading edge ionizes the gas. The laser light propagates in this plasma with a velocity equal to the group velocity

$$v_g \approx c \left[1 - \frac{\omega_{pe}^2}{2\gamma\omega_0^2} \right] \quad (1.48)$$

in a plasma, which, for plasma densities small compared to the critical density, is nearly equal to the velocity of the light. The short laser pulse has a strong intensity variation in time and correspondingly in space. This leads to a strong longitudinal ponderomotive force. The spatial extent of

this ponderomotive force, and that of the density perturbation caused by it, is of the order of $2c\tau$, where τ is the duration of the laser pulse. If this is made equal to the plasma wavelength ($\lambda_{pe} = 2\pi c/\omega_{pe}$), then high amplitude wakefields are produced due to quasi-resonance of the front push and the rear one. The wakefield moves with the pulse at a phase velocity equal to the group velocity of the laser pulse. Therefore, a correctly placed trailing bunch of relativistic electrons can be accelerated by the longitudinal field, with magnitude of 100 GV/m, of the plasma waves.

This model has already proven its validity, reaching accelerated electron bunch energy of 8 GeV [2]. However the poor quality of the bunch in terms of emittance and energy spread limits the possible applications.

One of the promising solution is to separate the wakefield generation and the injection mechanism. In the Resonant Multi-Pulse Ionization injection (ReMPI) scheme [3], for example, the idea is to excite the wake with a train of low-energy pulses separated in time by a plasma period. The wake excitation of each pulse resonantly adds, driving a final wakefield even stronger than in traditional Laser WakeField Acceleration (LWFA) (see FIG. 1.4). A second pulse, doubled or tripled in frequency, grants the ionization injection. Since a laser system capable of delivering the required pulse train should operate at a repetition rate of 100 GHz, not realistically feasible, it is necessary to generate such a train from a single high-energy pulse. At the beginning of chapter 3 an overview of proposed models is presented followed by an original design presented in this work.

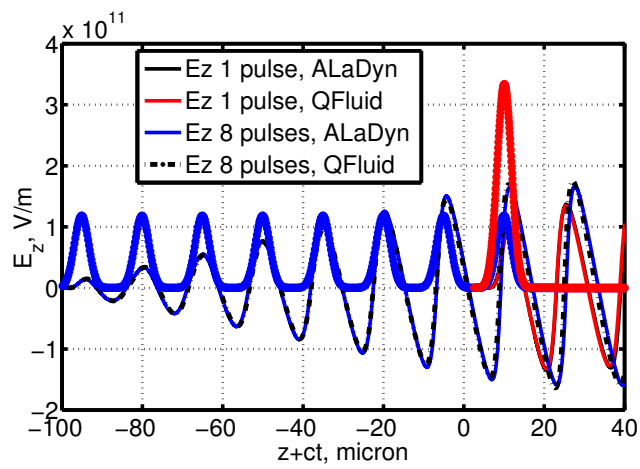


FIGURE 1.4: Comparison of wakefield excitation by a single pulse or a pulse train. In these plasma simulations pulses moving through the left are considered. The thin lines indicate the plasma wake. In this example a train of 8 pulses equally separated by the plasma period drives a wave (thin blue) whose maximum accelerating gradient is 20% more than that of the wave excited by the single pulse (thin red) with the same delivered energy. Figure from [3].

CHAPTER 2

THE E.M. FIELD IN THE FOCAL REGION OF AN OAP: A THEORETICAL MODEL AND A STUDY OF DEPOLARIZATION

As stated in the first chapter, in most of the laser-plasma experimental setups the laser beam is focused onto the target by an Off-Axis Parabola (OAP). This optical element is typically placed inside the interaction chamber and is the last one manipulating the laser beam. In these experiments the laser spot quality is checked throughout all the beam line steps but the dimension and intensity of the focused spot (of the order respectively of μm and $\geq 10^{18} \text{W/cm}^2$) make the experimental measurements difficult and inaccurate. Hence it is clear the importance of a thorough characterization by means of numerical simulations of the electromagnetic field produced by laser beam in the focus region of the OAP.

In this chapter a geometrical and theoretical model is developed, followed by a remarkable application in the field of laser-plasma acceleration, concerning intra-cycle depolarization. This theoretical scheme enables the numerical approach for the modelling of the *delay mask* presented in the next chapter.

2.1 GEOMETRICAL AND THEORETICAL FRAMEWORK

An Off-Axis Parabola is a mirror whose reflecting surface is a segment of a paraboloid, called *parent*, not containing its symmetry axis. FIG. 2.1(B) shows a real model of OAP available on the market. These devices are characterized by some parameters, provided by the manufacturing companies, such as off-axis angle, clear aperture, parent focal length and apparent focal length. Along with these geometrical quantities there are also other properties to consider when selecting an OAP such as material, coating, operational wavelength, optical properties in general, which are crucial in the context of a real experimental setup but in this thesis, where perfect reflection is assumed and surface degradation is not taken into account, are neglected.

After a brief introduction on previously developed models regarding electromagnetic field characterization of beam focused by parabolic mirror, a fully comprehensive geometrical and theoretical description is presented in order to clarify some concepts and introduce the operational framework.

2.1.1 OVERVIEW

The in-depth study on the structure of the electromagnetic field of beams focused by means of parabolic surfaces was initially undertaken in the field of optical microscopy, thus mainly concerning on-axis configurations. The earliest works were based on geometric optics approaches [18]. For example in [19] a mixed method is used: the beam is geometrically propagated from the parabolic mirror to a spherical surface which is then used as the boundary surface in a vector diffraction treatment based upon the Stratton-Chu theory [20].

The first studies based on a direct numerical integration of diffraction integrals, for either off-axis [21] or on-axis [22, 23] parabolic mirrors, date back to the early 2000s. Such approaches, made possible by the availability of advanced numerical integration schemes and increasingly powerful

simulation platforms, were driven by the need for tight focusing in various applications.

Motivated by the widespread diffusion of OAP as optical devices to focus ultrashort laser pulses, a growing attention is being devoted by the community of laser–matter interaction to the experimental and theoretical characterization of the intensity pattern in the focal region of high-intensity beams.

As it is known since the first works dealing with the focusing of ultrashort pulses by lenses [24], the envelope of the focused pulse takes on a rather complex structure in the far-field region, so that analytical frameworks able to predict the detailed electromagnetic field behaviour of an ultrashort pulse focused by an OAP would be desirable. However, as it can be easily realized, such treatments are rather cumbersome, due to both the ultrashort duration (implying large bandwidth) and the structure of the boundary surface (the parabolic mirror).

A theory enabling the study of the far field of femtosecond pulses focused by a parabolic mirror, although in an on-axis configuration, was recently presented in [25], aimed at investigating the ultimate intensity achievable under very tight focusing ($f/\# < 1$) with the next generation $\gtrsim 10$ PW systems. In particular, the authors first developed a theoretical treatment based on vector diffraction theory for a monochromatic wave upon reflection from the on-axis parabolic surface; based on that, the fields in the focal region of a femtosecond pulse are then calculated using a coherent superposition of monochromatic beams with suitable spectral amplitude and phase relationships.

A different approach was more recently proposed in [26]. The method provides an equation (for a Hertz-type vector potential) with the same structure of a unidirectional pulse propagation equation, which can be thus numerically solved using standard beam propagation methods. The reflection from an on-axis parabolic surface is taken into account using suitable initial conditions for the beam to be propagated. By comparison

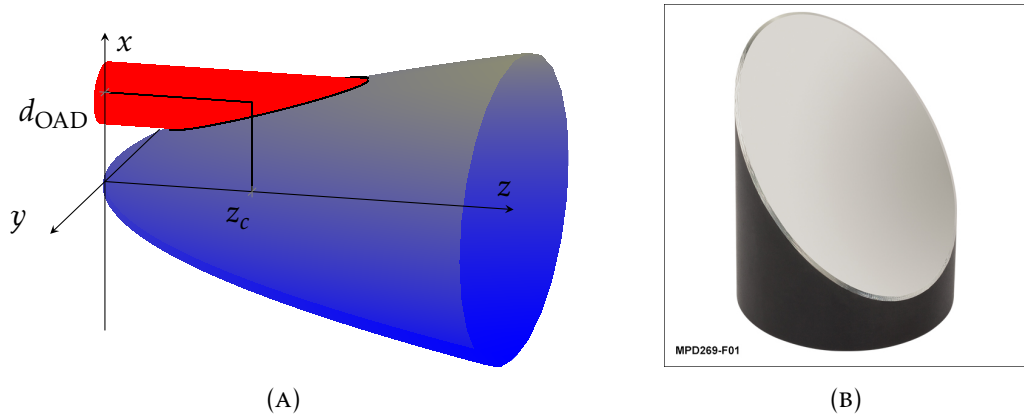


FIGURE 2.1: An off-axis parabola is geometrically defined (A) as the intersection between a cylinder and a paraboloid with non-coincident axes separated by a certain quantity d_{OAD} . (B) is a real commercial model of OAP mirror sold by the company Thorlabs.

with full vector diffraction calculations the authors find out that their method gives pretty accurate results down to $f/\# \sim 2-3$, while a 2-step method, involving the numerical integration of a diffraction integral, has to be used for smaller f-numbers.

In what follows an exact theoretical model is presented, based on a full vector diffraction treatment and also retaining the time dependence of the electromagnetic field as provided by its initial phase. This approach allows the electric and magnetic field of a beam focused by an OAP to be retrieved at any given time and space.

2.1.2 OFF-AXIS PARABOLIC MIRROR

A paraboloidal surface results, by definition, from the revolution of a planar parabola around its symmetry axis. Accordingly, the OAP surface (indicated hereafter by S_{OAP}), with circular aperture, results from the intersection of the above-mentioned paraboloid and a cylinder having its axis parallel (only coincident in the on-axis case) to the paraboloid one, as depicted in FIG. 2.1(A). The distance between the two axes is denoted by

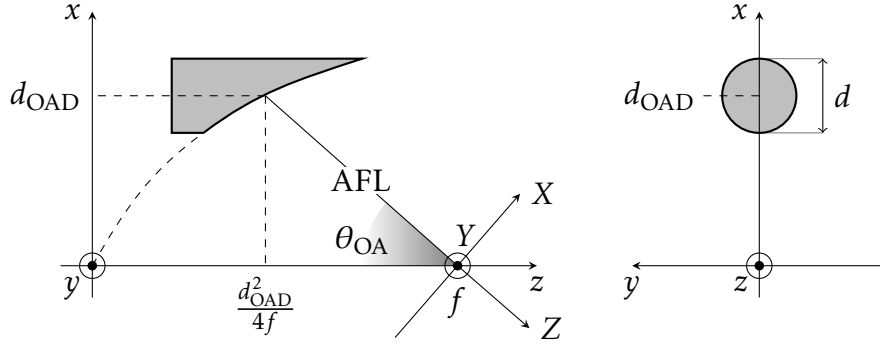


FIGURE 2.2: Meridional and sagittal sections of the geometry considered. The xyz coordinate system origin coincide with the paraboloid vertex. Every quantity is clearly labeled and the geometrical definitions are explained in the text.

d_{OAD} .

FIG. 2.2 provides the cartesian coordinate system considered, with the origin in the parent paraboloid vertex and the z axis coincident with the paraboloid axis, oriented in such a way that the focus point $\mathbf{x}_f = (0, 0, f)$ lays in the positive part of z , i.e. the focal length f is positive. With these conventions xz and yz planes are thus referred as the meridional and sagittal planes, respectively.

The equation of the paraboloid is then given by

$$z = \frac{x^2 + y^2}{4f} = a(x^2 + y^2) = s(x, y)f, \quad (2.1)$$

with $a = \frac{1}{4f}$ and $s(x, y) = \frac{a}{f}(x^2 + y^2)$ for later convenience. The OAP surface is defined by the condition

$$S_{\text{OAP}} : (x - d_{\text{OAD}})^2 + y^2 \leq \left(\frac{d}{2}\right)^2, \quad (2.2)$$

d being the diameter of the OAP. From a practical point of view, it is worth noticing that manufacturers call *diameter* the whole structure, i.e. the parabolic mirror and its housing, while *clear aperture* the area that actually interact with the light. In this thesis there won't be this difference and the diameter will be considered as the entire reflecting surface.

It is necessary now to calculate the area element and the normal to the surface. Equation (2.1) shows that, in cartesian coordinate, the parametric representation of the paraboloid depends on x and y . Thus the tangent vectors are

$$\mathbf{dr}_x = \left(1, 0, \frac{1}{2f}x\right) \quad \mathbf{dr}_y = \left(0, 1, \frac{1}{2f}y\right), \quad (2.3)$$

and for the surface element vector

$$d\mathbf{A} = \mathbf{dr}_x \times \mathbf{dr}_y = -\frac{1}{2f}x\hat{\mathbf{x}} - \frac{1}{2f}y\hat{\mathbf{y}} + \hat{\mathbf{z}}. \quad (2.4)$$

Finally, the area element and the unit inward, i.e. towards the focus point, vector are expressed as

$$dA = \sqrt{1 + s(x, y)} dx dy \quad (2.5)$$

$$\hat{\mathbf{n}} = \frac{1}{\sqrt{1 + s(x, y)}} \left(-\frac{x}{2f}, -\frac{y}{2f}, 1\right). \quad (2.6)$$

The quantity d_{OAD} has been already defined as the distance between the axes of the parental paraboloid and the boundary cylinder. The axis of this cylinder intercepts the OAP surface in what is defined as the *OAP center* $\mathbf{x}_c = (d_{\text{OAD}}, 0, ad_{\text{OAD}}^2)$. The distance between this point and the focus is called Apparent Focal Length (AFL) and it is the path length of an incoming ray parallel to the z axis, namely the *central ray*, impinging on the OAP center and focused in f .

Finally the off-axis angle θ_{OA} is introduced as the angle formed by the central ray with the z axis. It is simply calculated as

$$\theta_{\text{OA}} = \arctan \left(\frac{d_{\text{OAD}}}{f - \frac{d_{\text{OAD}}^2}{4f}} \right). \quad (2.7)$$

Since manufacturers typically differentiate and label the models in terms of the off-axis angle and the AFL we need another equation to fully calculate each quantity. From the geometrical definition of the parabola as the locus of points equally distant from the point f and the directrix

$z = -f$ (in the meridional plane) we have, considering the OAP center,

$$\text{AFL} = f + \frac{d_{\text{OAD}}^2}{4f}. \quad (2.8)$$

This equation along with eq. (2.7) form a closed system of equations from which the quantities f and d_{OAD} can be retrieved.

For later convenience, we will consider another cartesian coordinate system, obtained from the previous one by translating the origin into the focus point and rotating around the y axis by the off-axis angle. This system has the z axis parallel to central ray and the xy plane transverse to it and it is denoted in FIG. 2.2 by XYZ .

2.1.3 REFLECTED ELECTROMAGNETIC FIELDS

Now the general behavior of the electromagnetic fields and how they are reflected from the paraboloid surface will be discussed. We denote the incident electric and magnetic fields by \mathbf{E}_i and \mathbf{B}_i respectively, and assume perfect reflection, i.e. the 100% of the incoming radiation leaves the reflecting surface. Fields dependence on time and space has been omitted for clarity. In the discussion presented by VARGA and TÖRÖK in [22], it is stated that upon reflection the normal component of the electric field and the tangential component of the magnetic field remain unchanged. Recalling that $\hat{\mathbf{n}}$ is the direction vector of the reflected field, one may write

$$\mathbf{E}_{r,n} = \mathbf{E}_{i,n} = \hat{\mathbf{n}}(\hat{\mathbf{n}} \cdot \mathbf{E}_i) \quad (2.9)$$

$$\mathbf{B}_{r,t} = \mathbf{B}_{i,t} = \mathbf{B}_i - \mathbf{B}_{i,n}, \quad (2.10)$$

where the first subscript index indicates the incident (reflected) field i (r) while the second one the normal (tangential) component n (t). On the other hand, the tangential component of the electric field and the normal component of the magnetic field change sign, that is

$$\mathbf{E}_{r,t} = -\mathbf{E}_{i,t} = -(\mathbf{E}_i - \mathbf{E}_{r,n}) \quad (2.11)$$

$$\mathbf{B}_{r,n} = -\mathbf{B}_{i,n} = -\hat{\mathbf{n}}(\hat{\mathbf{n}} \cdot \mathbf{B}_i). \quad (2.12)$$

Combining eqs. (2.9) and (2.11) one obtains the total reflected electric field, and similarly for the total reflected magnetic field, expressed as

$$\mathbf{E}_r = 2\hat{\mathbf{n}}(\hat{\mathbf{n}} \cdot \mathbf{E}_i) - \mathbf{E}_i \quad (2.13)$$

$$\mathbf{B}_r = \mathbf{B}_i - 2\hat{\mathbf{n}}(\hat{\mathbf{n}} \cdot \mathbf{B}_i). \quad (2.14)$$

Finally one can write the total electromagnetic fields, i.e. incident and reflected, from the previous equations as

$$\mathbf{E} = \mathbf{E}_i + \mathbf{E}_r = 2\hat{\mathbf{n}}(\hat{\mathbf{n}} \cdot \mathbf{E}_i) \quad (2.15)$$

$$\mathbf{B} = \mathbf{B}_i + \mathbf{B}_r = 2\mathbf{B}_i - 2\hat{\mathbf{n}}(\hat{\mathbf{n}} \cdot \mathbf{B}_i), \quad (2.16)$$

where it is worth noticing that the total fields are expressed as function of the incident ones only.

2.1.4 FULL VECTOR DIFFRACTION MODEL FOR AN OAP

For a rigorous evaluation of the electromagnetic fields in focal region we use the Stratton-Chu vector diffraction theory [20] in this work. Such approach allows to fully characterize the spatial and temporal properties of the diffracted fields. As recently discussed in [27], Stratton-Chu theory allows, in general, the treatment of beam with sharp transverse profile, with respect to a more direct approach based on the Green's theorem applied to each field. In this work it is assumed that the reflection is always perfect, meaning that the totality of the fields scattered off the surface leaves the mirror.

Assuming that the electromagnetic field of the incident monochromatic laser beam can be formally factorized into the temporal and spatial domain, meaning that either domain is independent from the other, one can thus write

$$\mathbf{E}_i(\mathbf{x}, t) \equiv \mathbf{E}_i(\mathbf{x})e^{-i\omega t} \quad (2.17)$$

$$\mathbf{B}_i(\mathbf{x}, t) \equiv \mathbf{B}_i(\mathbf{x})e^{-i\omega t}, \quad (2.18)$$

where ω is the angular frequency of the beam, and treat the spatial part with the full vector diffraction theory provided by the Stratton-Chu equations.

Stratton-Chu formulation states that if the electric and magnetic fields are known on a closed surface A , then the diffracted fields are uniquely determined at a point \mathbf{x}_p in the far-field from the formulas:

$$\mathbf{E}(\mathbf{x}_p) = \frac{1}{4\pi} \int_A [ik(\hat{\mathbf{n}} \times \mathbf{B})G + (\hat{\mathbf{n}} \times \mathbf{E}) \times \nabla G + (\hat{\mathbf{n}} \cdot \mathbf{E})\nabla G]dA \quad (2.19)$$

$$\mathbf{B}(\mathbf{x}_p) = \frac{1}{4\pi} \int_A [ik(\mathbf{E} \times \hat{\mathbf{n}})G + (\hat{\mathbf{n}} \times \mathbf{B}) \times \nabla G + (\hat{\mathbf{n}} \cdot \mathbf{B})\nabla G]dA, \quad (2.20)$$

where $k = 2\pi/\lambda = \omega/c$ is the wavenumber of the incident beam. In these equations the contour term, i.e. the contour integral over the surface boundary, is omitted because it has been shown [22] to be negligible in the far-field calculation, which is the condition we are interested in. Here G is the Green function, solution of the Helmholtz equation¹, expressed as

$$G(\mathbf{x}) = G(\mathbf{x} - \mathbf{x}_p) = \frac{e^{ik|\mathbf{x}-\mathbf{x}_p|}}{|\mathbf{x} - \mathbf{x}_p|} \equiv \frac{e^{iku}}{u}, \quad (2.21)$$

where we defined $u = |\mathbf{u}| = |\mathbf{x} - \mathbf{x}_p|$, representing the distance between a point \mathbf{x} on the surface the integration is carried over and \mathbf{x}_p . The gradient of G can be easily calculated from the previous expression as

$$\begin{aligned} \nabla G &= \frac{iku e^{iku} - e^{iku}}{u^2} \left((x - x_p)\hat{\mathbf{x}} + (y - y_p)\hat{\mathbf{y}} + (z - z_p)\hat{\mathbf{z}} \right) \\ &= ik \left(1 - \frac{1}{iku} \right) \frac{G}{u} \left((x - x_p)\hat{\mathbf{x}} + (y - y_p)\hat{\mathbf{y}} + (z - z_p)\hat{\mathbf{z}} \right). \end{aligned} \quad (2.22)$$

In order to write the final integrals it is necessary to characterize the incident laser beam. We consider a monochromatic laser beam with a planar wavefront, a super-gaussian transverse profile, impinging on the

¹The Helmholtz equation represents the time-independent form of the wave equation and it is given by

$$(\nabla^2 + k^2)A(\mathbf{x}) = 0,$$

A being the amplitude.

OAP center with its axis parallel to the z axis. With this assumptions the fields can be written as

$$\mathbf{E}_i(\mathbf{x}, t) = A(x, y)e^{ikp(\mathbf{x})}(\cos \delta \hat{\mathbf{x}} + \sin \delta \hat{\mathbf{y}})e^{-i\omega t} = \mathbf{E}_i(\mathbf{x})e^{-i\omega t} \quad (2.23)$$

$$\mathbf{B}_i(\mathbf{x}, t) = A(x, y)e^{ikp(\mathbf{x})}(\sin \delta \hat{\mathbf{x}} - \cos \delta \hat{\mathbf{y}})e^{-i\omega t} = \mathbf{B}_i(\mathbf{x})e^{-i\omega t}, \quad (2.24)$$

with the amplitude on a generic reference plane given by

$$A(x, y) = A_0 \exp \left[-\frac{1}{2} \left(\left(\frac{x - d_{\text{OAD}}}{\sigma_x} \right)^2 + \left(\frac{y}{\sigma_y} \right)^2 \right)^n \right] \quad (2.25)$$

representing the super-gaussian profile of order n , shifted in the x direction in order to be coaxial with the OAP center. The angle δ is introduced to account for different polarization directions; in particular, $\delta = 0$ ($\delta = \pi/2$) corresponds to a linear polarization in the meridional (sagittal) plane. Finally, assuming as an arbitrary reference plane the one where the OAP center lays, the term

$$p(\mathbf{x}) = a(d_{\text{OAD}}^2 - (x^2 + y^2)) \quad (2.26)$$

represents the optical path difference between a point $(x, y, ad_{\text{OAD}}^2)$ on the reference plane and a point $(x, y, a(x^2 + y^2))$ on the OAP surface.

The fields inside eqs. (2.19) and (2.20) are the sum of the incident and reflected fields. Therefore, substituting eqs. (2.15) and (2.16) one gets

$$\mathbf{E}(\mathbf{x}_p) = \frac{1}{2\pi} \int_{\text{OAP}} ik(\hat{\mathbf{n}} \times \mathbf{B}_i(\mathbf{x}))G + (\hat{\mathbf{n}} \cdot \mathbf{E}_i)\nabla G \, dA \quad (2.27)$$

$$\mathbf{B}(\mathbf{x}_p) = \frac{1}{2\pi} \int_{\text{OAP}} (\hat{\mathbf{n}} \cdot \nabla G)\mathbf{B}_i(\mathbf{x}) - (\mathbf{B}_i(\mathbf{x}) \cdot \nabla G)\hat{\mathbf{n}} \, dA, \quad (2.28)$$

where S_{OAP} has been replaced by OAP for readability.

All the necessary quantities have been previously defined thus, after some cumbersome algebra, one gets a more explicit expression of the electromagnetic field components, considering also the time dependence,

in the form of

$$E_j(\mathbf{x}_p, t) = \frac{i}{\lambda} \iint_{\text{OAP}} g_{E_j}(\mathbf{x}, \mathbf{x}_p) A(x, y) e^{ik(u(\mathbf{x}, \mathbf{x}_p) + p(\mathbf{x}_p))} e^{-i\omega t} dx dy \quad (2.29)$$

$$B_j(\mathbf{x}_p, t) = \frac{i}{\lambda} \iint_{\text{OAP}} \frac{1}{u^2} \left(1 - \frac{1}{iku}\right) g_{B_j}(\mathbf{x}, \mathbf{x}_p) A(x, y) e^{ik(u(\mathbf{x}, \mathbf{x}_p) + p(\mathbf{x}_p))} e^{-i\omega t} dx dy, \quad (2.30)$$

with the index $j = x, y, z$ representing each cartesian component. The functions $g(\mathbf{x}, \mathbf{x}_p)$ can be written as

$$g_{E_x} = \frac{1}{u} \cos \delta - \frac{1}{u^2} \left(1 - \frac{1}{iku}\right) \left(\frac{x \cos \delta + y \sin \delta}{2f}\right) (x - x_p) \quad (2.31)$$

$$g_{E_y} = \frac{1}{u} \sin \delta - \frac{1}{u^2} \left(1 - \frac{1}{iku}\right) \left(\frac{x \cos \delta + y \sin \delta}{2f}\right) (y - y_p) \quad (2.32)$$

$$g_{E_z} = \frac{1}{u} \left(\frac{x \cos \delta + y \sin \delta}{2f}\right) - \frac{1}{u^2} \left(1 - \frac{1}{iku}\right) \left(\frac{x \cos \delta + y \sin \delta}{2f}\right) (z - z_p) \quad (2.33)$$

and

$$g_{B_x} = -\left(\frac{x \cos \delta + y \sin \delta}{2f}\right) (y - y_p) + \sin \delta (z - z_p) \quad (2.34)$$

$$g_{B_y} = \left(\frac{x \cos \delta + y \sin \delta}{2f}\right) (x - x_p) - \cos \delta (z - z_p) \quad (2.35)$$

$$g_{B_z} = -\sin \delta (x - x_p) + \cos \delta (y - y_p). \quad (2.36)$$

It is worth noticing that the g_E are complex-valued functions while the g_B are real-valued, basically due to the fact that the factor $\left(1 - \frac{1}{iku}\right)$ has been factorized.

Finally the real part of these fields, which is the pivotal quantity to be evaluated from an experimental point of view, can be readily written as

$$E_j^{(r)} = -\frac{1}{\lambda} \iint_{\text{OAP}} \left(g_{E_j}^{(r)} \sin(kv - \omega t) + g_{E_j}^{(i)} \cos(kv - \omega t)\right) A dx dy \quad (2.37)$$

$$B_j^{(r)} = -\frac{1}{\lambda} \iint_{\text{OAP}} g_{B_j} \frac{1}{u^2} \left(\sin(kv - \omega t) + \frac{1}{ku} \cos(kv - \omega t)\right) A dx dy, \quad (2.38)$$

where $v(\mathbf{x}, \mathbf{x}_p) = u(\mathbf{x}, \mathbf{x}_p) + p(\mathbf{x}_p)$. The notation $f^{(r)} \equiv \text{Re}(f)$ and $f^{(i)} \equiv \text{Im}(f)$ denotes respectively the real and the imaginary part of a complex function. In what follows the real part notation is omitted for readability.

Equations (2.37) and (2.38) allow the calculation of the electric and magnetic field reflected by an OAP at any time, meaning also at a sub-cycle level, and space. Although this model doesn't provide an analytically closed set of expressions, thus requiring a numerical computation, it is an original developed work that doesn't present any approximation or Taylor expansion, retaining a general validity for many different applications.

2.2 NUMERICAL INTEGRATION

The main goal of the model presented in the previous section is to allow the computation of the three-dimensional electromagnetic field components in order to fully characterize focused beams and study their behavior in different situations. For this purpose it has been necessary to develop an original C++ code, chosen for its fast computational power with respect to high level numerical softwares, such as Mathematica.

It is useful to define some parameters in order to clarify how the algorithm has been implemented. The following subsections concern the non-trivial input parameters and explain how all the quantities necessary to the electromagnetic field computation are retrieved.

FWHM

The parameter spatially defining the super-gaussian laser beam is the FWHM, as depicted in FIG. 2.3. It, quite literally, indicates the transverse region where the amplitude of the beam is at least half of its maximum. Recalling the super-gaussian spatial amplitude profile expressed by eq. (2.25) and assuming rotational symmetry in respect to its axis, one can write

$$\sigma_x = \sigma_y \equiv \sigma = \frac{\text{FWHM}}{2(\ln 2)^{\frac{1}{2n}}}. \quad (2.39)$$

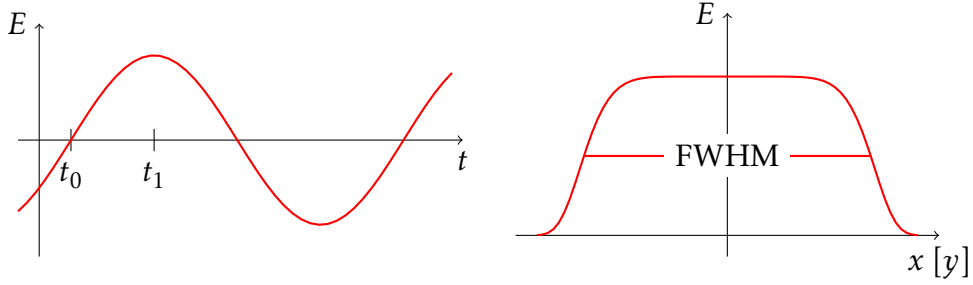


FIGURE 2.3: Spatial and temporal form of the incident laser beam.

TIME

Assume that t_0 and t_1 indicate the time at which the field reach, respectively, the zero and the maximum value within the optical cycle (FIG. 2.3). In particular eq. (2.37) can be used to evaluate the time t_0 at which the field of the reflected central ray vanishes at the focus point.

Consider, for simplicity and without losing generality, a monochromatic laser linearly polarized along the y axis ($\delta = \frac{\pi}{2}$), with $A_0 = 1$. For the electric field to be null it must be

$$g_{E_y}^{(r)} \sin(kv - \omega t) + g_{E_y}^{(i)} \cos(kv - \omega t) = 0. \quad (2.40)$$

Recalling that

$$g_{E_y}^{(r)} = \frac{1}{u} - \frac{y}{2f} \frac{y - y_p}{u^2} \quad g_{E_y}^{(i)} = -\frac{y}{2f} \frac{1}{ku} \frac{y - y_p}{u^2} \quad (2.41)$$

and that we are considering only the central ray, i.e.

$$\mathbf{x} = (d_{\text{OAD}}, 0, ad_{\text{OAD}}^2) \quad \mathbf{x}_p = (0, 0, f), \quad (2.42)$$

it can be written

$$\tan(kv - \omega t) = -\frac{g_{E_y}^{(i)}}{g_{E_y}^{(r)}}. \quad (2.43)$$

The numerator on the right is identically zero thus

$$\tan(kv - \omega t) = 0 \Rightarrow kv - \omega t = n\pi, \quad (2.44)$$

and finally, taking $n = 0$, after substituting the known quantities,

$$t_0 = \frac{1}{c} \sqrt{d_{\text{OAD}}^2 + (ad_{\text{OAD}}^2 - f)^2}. \quad (2.45)$$

It can also be readily verified that

$$t_1 = t_0 + \frac{T}{4} = t_0 + \frac{\pi}{2\omega}, \quad (2.46)$$

T being the radiation period, easily retrievable from the laser wavelength λ provided as another input parameter. Even further, it is possible to investigate any time point of interest within the optical cycle using the calculated t_0 as reference.

OFF-AXIS ANGLE AND F-NUMBER

The values of d_{OAD} and f are calculated, as mentioned before, as the solutions of the system

$$\begin{cases} \theta_{\text{OA}} = \arctan\left(\frac{d_{\text{OAD}}}{f - \frac{d_{\text{OAD}}^2}{4f}}\right) \\ \text{AFL} = f + \frac{d_{\text{OAD}}^2}{4f}. \end{cases} \quad (2.47)$$

The off-axis angle θ_{OA} is an input parameter while AFL depends on the f-number, formally defined as

$$f/\# = \frac{\text{FWHM}}{\text{AFL}}, \quad (2.48)$$

Low f-numbers simply indicate short focal, typically used in ion acceleration experiments, while high f-numbers indicate more depth of focus, which is usually better for electron acceleration.

Another input parameter is the integration domain. Since the Stratton-Chu integrals are bi-dimensional, the intervals of only the x and y variable need to be set and are chosen to be $2 \times \text{FWHM}$, centered in $(d_{\text{OAD}}, 0)$.

Finally, the focal plane, i.e. the plane perpendicular to the reflected beam and centered at focus, consists of a square grid of points which side

also depends on the f-number. The focused beam waist is taken to be $1.22 \times \lambda \times f/\#$ and therefore the square size is set to approximately double the beam waist. The grid sample has a fixed value of 1600 points therefore the resolution varies with the f-number too.

The proper numerical integration is performed using cubature library². This library implements a multi-dimensional adaptive integration scheme based on the algorithm described in [28]. The evaluation of each integral is stopped when it reaches a relative error of 10^{-6} , i.e. when the computed error is less than the integral value $\times 10^{-6}$.

All quantities are evaluated in the xyz coordinate system but, since one is in general interested in study the electromagnetic field along the longitudinal and transverse directions with respect to the focused beam propagation direction, it is useful to retrieve them in the XYZ system (see FIG. 2.2). This can be easily achieved considering a rotation matrix around the y axis:

$$\begin{bmatrix} E_X \\ E_Y \\ E_Z \end{bmatrix} = \begin{bmatrix} \cos \theta_{OA} & 0 & \sin \theta_{OA} \\ 0 & 1 & 0 \\ -\sin \theta_{OA} & 0 & \cos \theta_{OA} \end{bmatrix} \begin{bmatrix} E_x \\ E_y \\ E_z \end{bmatrix}. \quad (2.49)$$

When the code is launched it loads all the previously described parameters and performs the integrations for each field component (3 for the electric field and 3 for the magnetic one) for every points on the focal plane grid. On a commercial Intel-i7 laptop with Linux based operating system, each computation typically takes a few hundreds of milliseconds resulting in approximately 20 minutes per simulation, which is considered a reasonable amount of time for a full vector diffraction scheme.

2.3 INTRA-CYCLE DEPOLARIZATION

The validity of the model, and its code implementation, described in the previous sections are generic enough to enable all sorts of different analysis

²<https://github.com/stevengj/cubature>

concerning the electromagnetic field of a laser beam focused by an OAP. In addition to its usefulness in the designing part of the mask presented in this work, we also employed the simulation code in the investigation upon the recently discussed phenomenon of polarization loss at a sub-cycle level for a beam focused by an OAP.

2.3.1 OVERVIEW

A recent paper by LABATE *et al.* [29] displays the effects of small misalignments on the intensity of a laser beam focused by an OAP, enhancing the crucial role of the parabola in regard to focal spot quality. This could raise the question: could the OAP also affect the polarization of the focused beam?

Recent works [30–32] reported on an experimental setup capable of characterize a THz beam focused by a 90° OAP with a sub-cycle resolution. In these studies the authors observed a loss of the original polarization structure and the formation of anomalous electromagnetic pattern at the time of the optical cycle at which the fields are supposed to vanish. They also developed an approximate model capable of predicting the loss of polarization but the lack of a thorough theoretical approach makes this model valid only in specific setups.

Actually the idea that the polarization could not be preserved in the case of off-axis focusing dates back to 1987 [33]. The model presented in this work predicts a smooth spatial dependence of the polarization in the focal plane due to an off-axis ellipsoidal mirror. However this statement only concerned the time averaged pattern of the polarization direction, without taking into account any sub-cycle behaviour.

The aim of the following simulations is to exploit the comprehensive theoretical model previously developed and actually show, at a sub-cycle level, this depolarization effect.

TABLE 2.1: Values of the parameters used in the simulations. They are chosen to be comparable to realistic experimental setups.

Parameter	Symbol	Value
Wavelength	λ	800 nm
Super-gaussian index	n	4
Constant amplitude	A_0	1
Beam extension	FWHM	40 mm

2.3.2 SIMULATIONS

Some parameters are fixed throughout the entire set of simulations and, for the sake of comparison with a realistic experimental setups, are chosen to represent the typical laser beam generated in up-to-date facilities. They are displayed in TAB. 2.1 and their role is described in section 2.2.

In order to examine this alleged depolarization effect the idea is to plot and compare the transverse electromagnetic vector field on the focal plane at t_0 and t_1 , the time, within the optical cycle, at which the focused beam has the minimum and the maximum amplitude, respectively (see FIG. 2.3). More clearly (since this is a pivotal definition in all the following discussions), t_0 is the time at which either the electric and the magnetic field of the focused beam, as expressed by eqs. (2.37) and (2.38), at the center of the focal plane are supposed to vanish; on the other hand at t_1 the fields take on their maximum amplitude. The original polarization direction δ , the off-axis angle θ_{OA} and the f-number $f/\#$ are taken to be the independent variables.

Most of the reported plots represent the behaviour of different fields in a plane XY orthogonal to the reflected central ray (refer to the coordinate system XYZ shown in FIG. 2.2) where the point $(0,0)$ is the focus of the OAP. With these assumptions we indicate as transverse electric and

magnetic field the vectors

$$\mathbf{E}_{\text{tr}} = \mathbf{E}_X + \mathbf{E}_Y \quad (2.50)$$

$$\mathbf{B}_{\text{tr}} = \mathbf{B}_X + \mathbf{B}_Y. \quad (2.51)$$

Unless otherwise specified, vectors' amplitude in the vector maps of the electromagnetic field are normalized to 1, meaning that they are to be intended as relative to E_{max} , defined as

$$E_{\text{max}} \equiv \max \mathbf{E}_{\text{tr}} \Big|_{t_1}, \quad (2.52)$$

i.e. the maximum value of the transverse electric field evaluated at t_1 . The same stands for the magnetic field. Moreover, for graphical purpose, vectors length is set not to be longer than the grid of the focal plane $\Delta X (= \Delta Y)$.

Also, recalling that

$$I \propto |\mathbf{E}|^2, \quad (2.53)$$

we will improperly (since we are not accounting for a time dependence) use the term *intensity* to refer to the electromagnetic energy density.

As a reference case, and also in order to stress the role of the off-axis angle, we consider a linearly polarized beam along the x axis, i.e. $\delta = 0$, impinging on a $f/2$ parabolic on-axis mirror. The resulting transverse electric and magnetic fields are displayed in FIG. 2.4. The on-axis configuration shows the expected behaviour: the fields vanish at t_0 , as much as 4 order smaller than the maximum, at most, and, more importantly, they retain the original polarization.

Consider the same set of parameters as the previous reference case with the only exception of the off-axis angle, which is now set to be $\theta_{\text{OA}} = 40^\circ$. Plots in FIG. 2.5 display completely different results which need to be discussed. FIG. 2.5(B) shows the transverse electric field at t_1 of the focused beam. As expected, due to the original polarization along the x axis, it is directed in the X direction. In the same way the transverse magnetic field, perpendicular to the electric one, retain the original direction along

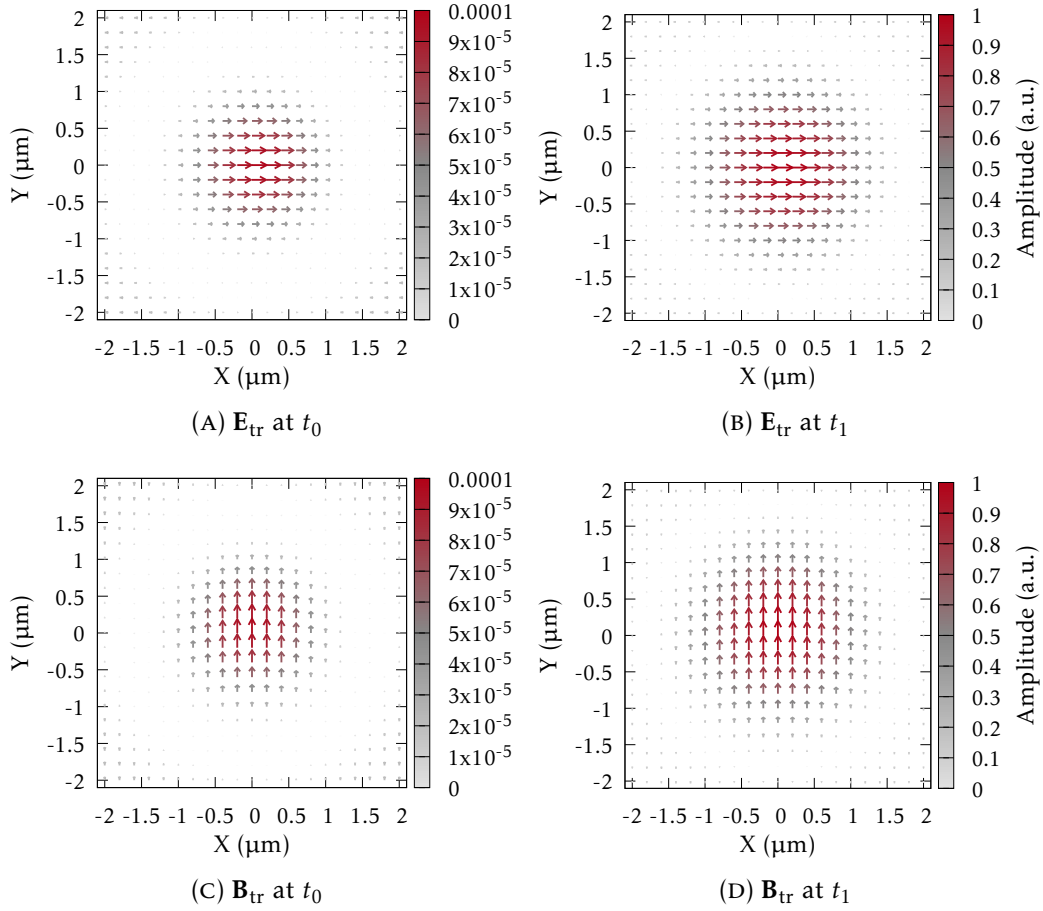


FIGURE 2.4: Transverse electric ((A) and (B)) and magnetic ((C) and (D)) vector fields at t_0 and t_1 for $\delta = 0$, $f/2$ and $\theta_{\text{OA}} = 0^\circ$. Amplitude is relative to E_{max} (definition in text). In the on-axis case it can be seen, as expected, that the fields vanishes at t_0 and that the polarization is preserved.

the Y axis. Looking at the plots for t_0 , though, an anomalous effect can be observed. Both the electric and magnetic field actually vanish only at the focus point, the central one, while in its proximity a complex, not obvious, pattern appears. Indeed, considering the electric field, a completely 90° turn in the polarization can be observed along the Y axis. The field amplitude of this unusual components are, at most, the 3.5 % of E_{\max} , as can be seen from the color scale of the plots. One could tag it as a negligible effect but since focusing by OAP is typical of high-energy experiments, where the polarization also has an important role, it is, at least, an effect to account for in specific circumstances. Later it will be shown how the magnitude of this effect depends upon the OAP parameters such as the f-number and the off-axis angle.

Having established the expected orthogonality between the electric and the magnetic field, all of the following discussions and analysis will refer, for the sake of conciseness, exclusively to the electric field. Hence it is to be inferred that the same conclusions will obviously stand also for the magnetic field.

At this point, it could be interesting to investigate the behaviour of the fields in the proximity of t_0 , meaning the time steps immediately before and after it. Consider the case with $\delta = 0$, $f/2$ and $\theta_{\text{OA}} = 40^\circ$. Indicating with T the radiation period, two simulations are carried: one at $t_0 - T/200$ and one at $t_0 + T/200$, a time span that, in the studied case, corresponds to a few attoseconds. The results, always plotted as the vector map of the transverse electric field at the focal plane, are shown in figs. 2.6(a) and 2.6(b), respectively. As it can be easily noticed from the figures, the region where the field actually vanishes describe a sort of sweep along the X axis. What emerges is that a small neighbour of points in the meridional plane exists where, at times close to t_0 , the electric field vanishes; for the exact instant t_0 the field vanishes only at the focal point.

For further analysis, let's now introduce the concept of Region Of Interest (ROI). It is defined as the region over which the focused beam intensity

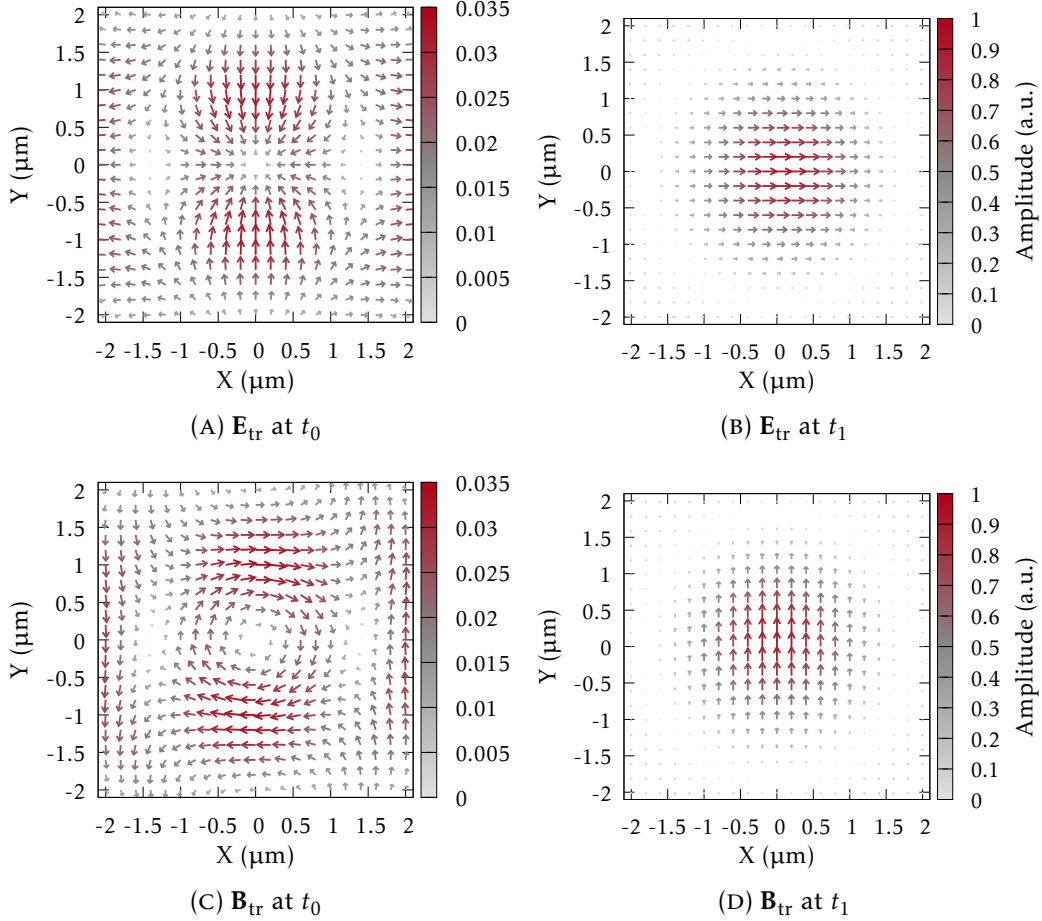


FIGURE 2.5: Transverse electric ((A) and (B)) and magnetic ((C) and (D)) vector fields at t_0 and t_1 for $\delta = 0$, $f/2$ and $\theta_{\text{OA}} = 40^\circ$. Amplitude is relative to E_{max} (definition in text). At t_0 the introduction of an off-axis angle is responsible for an unusual vector pattern around the focal point (the only one where the fields actually vanish) where the initial polarization is not preserved. Even if the amplitude is 2 order of magnitude lower with respect to t_1 , it is not a negligible effect due to the energy involved.

has a magnitude of at least 10 % of the maximum intensity. In other words, the grid points fulfilling this minimum-intensity requirement are considered while the others are set to 0. Beside enabling a better readability of the plots, this selection procedure permits to focus only onto the spatial region where the unusual field observed at t_0 has enough magnitude to potentially lead to non negligible effects in real-plasma interaction experiments.

It is now easier to estimate other effects due to the OAP focusing. For instance, it is worth to mention that a longitudinal electric field component is also appearing at t_0 . Restricting the attention to the abovementioned ROI it is possible to plot a density map of the ratio of the longitudinal component E_Z to the transverse component $E_{\text{tr}} \equiv |\mathbf{E}_{\text{tr}}|$ at t_0 . The map is displayed in FIG. 2.6(C) and, compared to the top plots of FIG. 2.5, highlights the appearance of a longitudinal component in the region where the transverse component is smaller, except for the neighbour of the central point.

2.3.3 PARAMETRIC DEPENDENCE OF THE DEPOLARIZATION

The developed model allowed a full numerical characterization of this depolarization effect, in agreement with the experimental evidence. In order to generalize the discussion and break free from the single simulation parameters, we investigate how the unusual field patterns depend upon the OAP parameters, namely the off-axis angle and the f-number.

To this purpose, the ratio of the square modulus of the electric field transverse component E_{tr}^2 at t_0 to the respective quantity at t_1 is first considered. An example of this map, restricted to the previously defined ROI and with the usual parameters $\delta = 0$, $f/2$ and $\theta_{\text{OA}} = 40^\circ$, is reported in FIG. 2.6(D). Recalling that in the on-axis case the fields almost vanish across the entire focal plane, it is clear that the effect observed in this map is specifically a consequence of the OAP focusing properties. Such map is capable of displaying both the spatial distribution of the anomalous field and its magnitude, relative to the normal one at t_1 . From the comparison

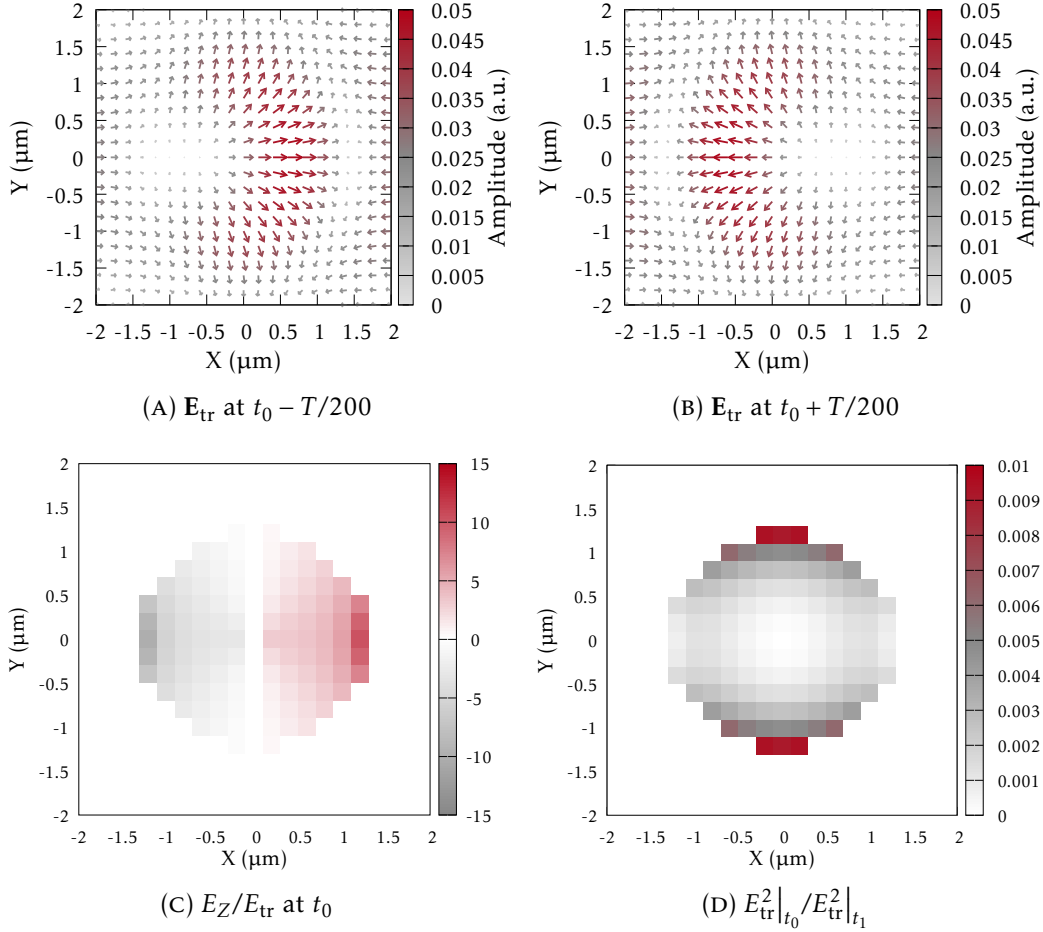


FIGURE 2.6: The maps on top represent the transverse electric vector field immediately before and after t_0 for $\delta = 0$, $f/2$ and $\theta_{\text{OA}} = 40^\circ$ (same parameters for the other plots); the amplitude is relative to the maximum transverse field at t_1 . In (C) the ratio of the longitudinal electric field component to the transverse one at t_0 is displayed, while in (D) the ratio of the square modulus of the transverse field at t_0 to the corresponding value at t_1 .

of the maps (here not reported for readability) relative to different off-axis angles and f-numbers it is evident that these parameters play a role in the anomalous field properties.

FIG. 2.6(D) makes clear that the relative magnitude of the anomalous field is not uniform across the ROI. Thus, for a quantitative assessment of the depolarization dependence upon the OAP parameters, it is necessary to define a spatially averaged quantity. For instance, consider the integral of the square modulus of the transverse electric field averaged over the ROI, using the local intensity as weight; in formula

$$\langle E_{\text{tr}}^2 \rangle = \frac{\int_{\text{ROI}} E_{\text{tr}}^2 I(X, Y) dX dY}{\int_{\text{ROI}} I(X, Y) dX dY}. \quad (2.54)$$

It is now possible to define a parameter κ as the ratio of the average transverse field at t_0 to the corresponding value at t_1 :

$$\kappa := \frac{\langle E_{\text{tr}}^2 \rangle|_{t_0}}{\langle E_{\text{tr}}^2 \rangle|_{t_1}}. \quad (2.55)$$

In other words, this parameter, from its definition, indicates how important, how relevant in the a particular configuration, the anomalous field is; investigating its dependence upon OAP parameters can even lead to the formulation of some scaling laws.

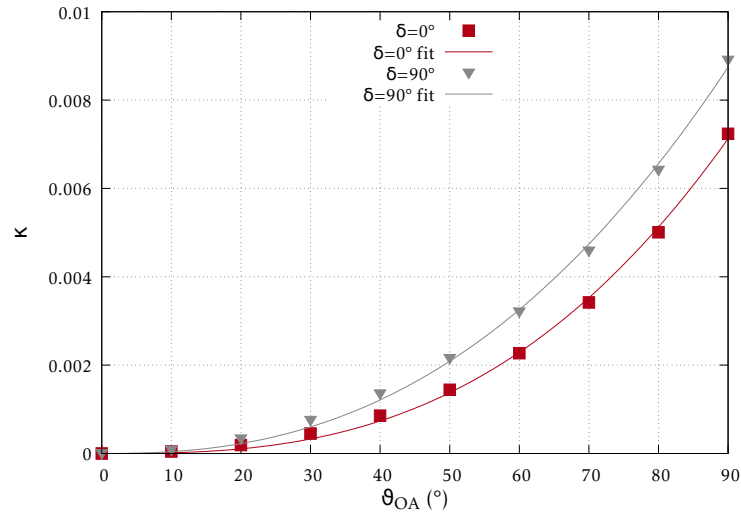
In particular, running several simulations, letting one parameter at a time to vary, it is possible to plot the κ parameter as a function of the off-axis angle (FIG. 2.7(A)) and of the f-number (FIG. 2.7(B)). Fitting the data with the following scaling laws

$$\kappa \propto (\theta_{\text{OA}})^\alpha \quad (2.56)$$

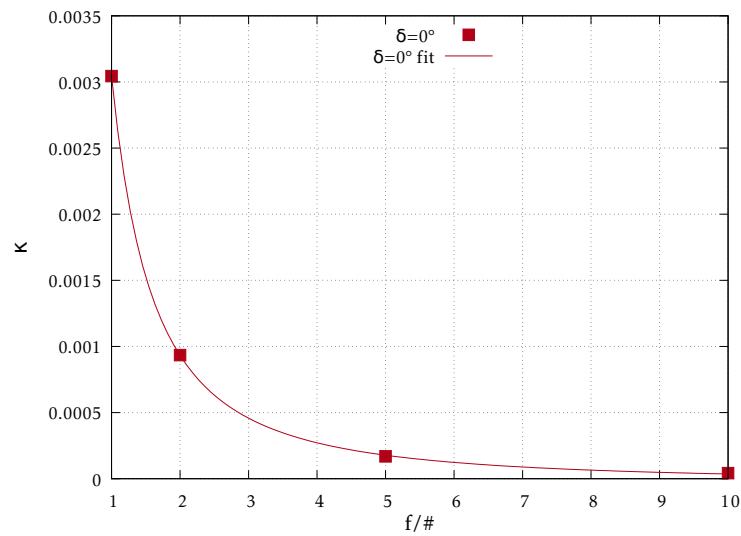
$$\kappa \propto \frac{1}{(f/\#)^\beta}, \quad (2.57)$$

yields, for the polarization along the x axis, $\alpha \simeq 2.79$ and $\beta \simeq 1.68$. Furthermore in FIG. 2.7(A) is also highlighted a difference between the two orthogonal polarization of the incoming beam: in fact, for the y polarization, the fit yields $\alpha \simeq 2.81$. In words, these plots clearly indicate that

the depolarization effect becomes particularly evident for high off-axis angle and for tight focusing, which is typically the arrangements needed in proton acceleration experimental setups. On the other hand, this phenomenon is expected to be negligible for high f-number optics, which are more commonly employed in LWFA experiments.



(A) Off-axis dependence



(B) F-number dependence

FIGURE 2.7: Plots and fits of the κ parameter (see the definition in text) depending upon the off-axis angle and the f-number. The fixed parameters in (B) are $\delta = 0$ and $\theta_{OA} = 40^\circ$. In (A), evaluated for $f/2$, the difference between the two orthogonal polarizations is also displayed.

A SIMPLE EXPERIMENTAL METHOD FOR PULSE TRAIN GENERATION: THEORETI- CAL STUDY

Plasma wakefields in LWFA experiments are typically excited by a single high-energy ultrashort pulse. This technique has already proven its validity, delivering accelerated electron bunch with energy up to 8 GeV [2]. However poor bunch quality, in terms of emittance and energy spread, limits possible applications of laser-plasma acceleration, e.g. Free Electron Laser (FEL).

Some recently published works [3, 34] turned their attention to Multi-Pulse Laser WakeField Acceleration (MP-LWFA). This model, obviously derivative of LWFA, employs a train of lower-energy pulses to resonantly excite the plasma wakefield, instead of a single high-energy one. The main requirement for this scheme is to have the subpulses delayed one from the each other by the plasma period. In the ReMPI scheme, for example, a laser system capable of delivering such train should operate at a repetition rate of 100 GHz. Consequently the most efficient and immediate solution is to generate the pulse train from the single high-energy ultrashort laser pulse already in use in existing LWFA experiments.

As a simple method of pulse train generation we propose the use of a

delay mask: an optical component, placed on the beam line right before the last focusing optic, typically an OAP, delaying different parts of the original beam, that will finally result in a train of pulses at the focal plane of the OAP, where the target is usually placed.

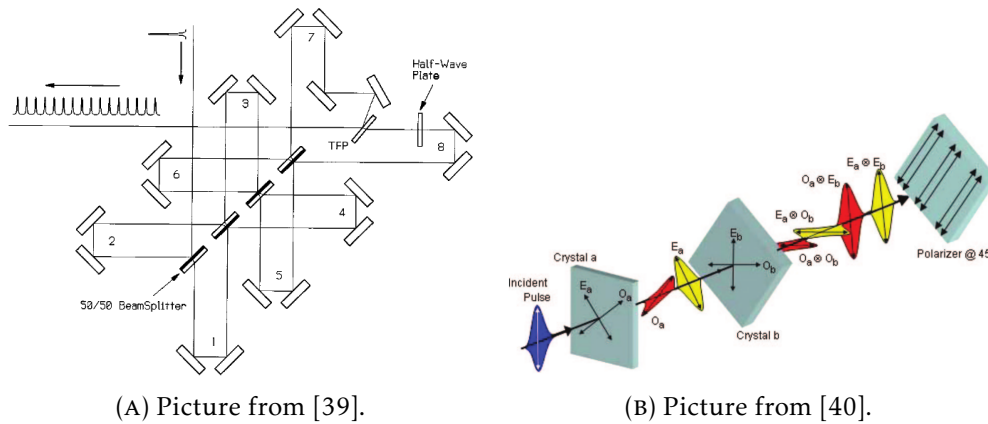
In this chapter the delay mask is presented, from the initially dismissed designs to the final model. Geometrical dimensions of the mask depend, aside from the manufacturing capabilities, on both the spatial and temporal properties of the pulse train we need to obtain. The spatial characterization at the focal plane of the electromagnetic field of each pulse in the train is provided by the numerical method displayed in chapter 2. Dispersion theory together with Miro software provide instead the temporal characterization.

3.1 THE IDEA

As mentioned in the first chapter, MP-LWFA is recently getting a renewed interest since its first theoretical description in the early 90s [35, 36]. At the moment the greatest limitation is due to the lack of an efficient and reliable method of generating a suitable pulse train. Thus, preliminary tests and experimental proofs of principle of MP-LWFA require the pulse train to be somehow generated from the single high-energy ultrashort laser pulse available in classical LWFA experiments.

3.1.1 PULSE TRAIN GENERATION

In order to better understand the model presented in this thesis, it is important to briefly discuss previously proposed methods. In the last two decades the generation of a pulse train from a single laser pulse has been widely investigated. In addition to the already mentioned laser-plasma accelerators, other field boosted this line of research such as excitation of atoms, molecules and solids [37] and radar/microwave communication technologies [38].



(A) Picture from [39].

(B) Picture from [40].

FIGURE 3.1: First proposed logarithmic devices of pulse train generation from a single laser pulse. In (A) the train results from a sequence of Michelson interferometers, introducing an adjustable delay via path differences. In (B) the train comes from an array of subsequent birefringent crystal where the difference in group velocities for the ordinary and extraordinary polarization state generates the required delay.

One of the first proposed models was based on stacked Michelson interferometers [39]. What *stacked* means is that an initial single pulse impinge on a first beam splitter, the output of which is redirected to a second one and so on. The idea is to use both beams from each beam splitter, recombine them at the end of the Michelson array via polarization multiplexing and thus obtaining a pulse train with nearly 100% throughput. The spacing between each pulse depends on the adjustable path difference of the delay arms and it is claimed to be ranging continuously from zero to few nanoseconds. FIG. 3.1(A) represents an example device providing a train composed by 16 pulses. As also evident from the figure, such scheme can generate a train with 2^n pulses employing a significant amount of optical elements: n beam splitter, $(4n + 2)$ mirrors, $2n$ linear translators, 1 half-wave plate and 1 thin-film polarizer.

On the same line of *logarithmic*¹ devices, another model was presented

¹The term generically refers to the fact that the employment of n devices generates a train composed by 2^n pulses, hence obeying to a logarithmic law.

in [40], making use of the optical properties of birefringent crystals. These crystals are characterized by having two orthogonal optical axes with different refractive indexes, namely ordinary (n_o) and extraordinary (n_e). A single pulse propagating through such medium is then split into two, depending on the polarization directions with respect to the optical axes of the crystal. Thus, for a given thickness x of the material, a temporal delay Δt resulting from the different group velocities of the two polarizations (v_o for the ordinary and v_e for the extraordinary one) can be introduced between the two pulses such that

$$\Delta t = x \left(\frac{1}{v_o} - \frac{1}{v_e} \right). \quad (3.1)$$

FIG. 3.1(B) depicts an example configuration for producing a train of 4 pulses. A linear polarizer at the end of the beam line is needed, despite the introduction of $\sim 50\%$ energy loss, in order to grant a single polarization state for the pulse train. With this scheme an array of n birefringent crystals, each with sequentially doubled thickness, can produce a pulse train of 2^n pulses.

More recently, a technique involving spectral filtering of chirped pulses has been investigated. In particular in [41] the authors display two setups: a combination of a Multi-order Wave Plate (MWP) and a linear polarizer, as a refinement of the work presented in [42], and a single Michelson interferometer. In the first one, all of the incident energy is used to generate two, co-propagating pulse trains with a controllable spacing between them. A chirped linearly polarized pulse is passed through a MWP with its axes at 45° . The transmitted pulse is then directed to a thin-film Polarizing Beam-Splitter (PBS), which reflects (transmits) the parallel (perpendicular) polarized components of the pulse. Both components are then retro-reflected by a pair of mirrors to the PBS. This arrangement yields two, orthogonally-polarized pulse trains containing all of the initial energy. The retro-reflecting mirrors in the transmitted arm are mounted on a translation stage, thus allowing the spacing between the pulse trains to be

controlled. In the configuration with only one Michelson, spectral filtering of a chirped pulse can be achieved simply by considering the optical path difference Δx . Indeed it causes a phase delay of

$$\Delta\phi = \frac{2\pi}{\lambda}\Delta x. \quad (3.2)$$

When the two pulses recombine at the beam splitter, wavelengths for which the total phase difference is an even integer multiple times π will be transmitted to the output without any loss. It will therefore convert a linearly-chirped pulse to a pulse train containing half of the incident energy, with a temporal profile equal to that of the incident pulse modulated by a cosine-squared function.

This last setup was implemented in a recent laser-plasma acceleration experiment [43], in which the Michelson is placed along the beam line between the final laser amplifier and its vacuum compressor. In this case, with the compressor set for partial compression, the modulated spectrum transmitted by the Michelson is partially compressed to a train of pulses, with a temporal spacing which can be controlled by adjusting the delay arms of the Michelson and compressor. As claimed in the paper, this was the first experimental demonstration of MP-LWFA, where the wakefield was excited by a laser pulse structure which is long compared to the plasma period. The results shown, together with the ability to deliver the driving laser energy over many plasma periods, encourage not only the development of high-repetition-rate laser systems but indicate also a route to achieving better accelerated bunch quality in external injection schemes.

The previously described models offer pros and cons but they all share the need of a fair amount of additional optical elements. From a physical point of view this isn't necessarily an issue, albeit requiring particular attention to the beam quality and characterization throughout the entire line, but cost-wise it adds a significant amount of expenses the laboratories, especially the small ones, need to account for. Moreover, from a practical perspective, the properties of a high-energy ultrashort pulse make the

alignment process particularly sensitive and time-consuming, scaling of course with the number of additional optics.

3.1.2 THE DELAY MASK

The development process of a novel system for generating the pulse train took its initial steps from the final considerations on the previously described models. Furthermore, in the context of the ReMPI scheme (see section 1.4.1) none of them meet the requirements of high efficiency and reduced amplitude variations among the different pulses of the train. So, focusing on a cost-effective solution, simple to be implemented in existing LWFA experiments, and suitable for the ReMPI operational framework, the choice landed on a *delay mask*.

More clearly, the idea is to put a passive optical component, with particular geometrical shape and dimensions (to be later determined), onto the beam line right before the last focusing element, typically an OAP. This component should have transverse (with respect to the beam propagation direction) regions of various thickness. A laser beam impinging on it is split in the sense that each part emerging from the corresponding region is temporally separated from the other due to the delay introduced by the propagation through different material lengths. These transverse sections of the laser pulse will be finally focused onto the target by the OAP, generating at the focal region a train of pulses. In summary, we investigate the feasibility of this simple concept, exploiting the velocity of laser pulse propagating through matter and taking into account dispersion effects.

3.2 SPATIAL CHARACTERIZATION

The main issue in choosing the transverse shape of the mask concerns the focused spot of each part of the laser. From now on assume that after the mask the beam, or rather all of the beam parts, will encounter only the focusing OAP. In this way the characterization of the spots depends

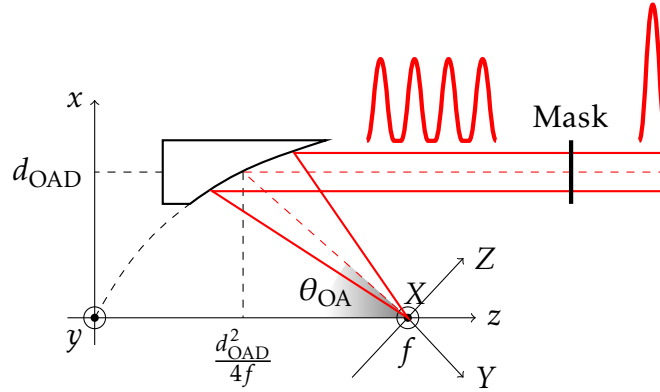


FIGURE 3.2: Geometrical model for the train simulations. An initial single pulse impinges onto the delay mask consisting of 4 transverse, with respect to the pulse propagation direction, sections of different thickness, thus delaying the emerging parts one from the other. Each of them is then focused by the OAP resulting in a pulse train at the focal plane.

solely on how these beam parts are focused by the OAP. Since, in principle, the regions can have any complicated forms it is difficult to analytically evaluate the focused electromagnetic fields. Thus we employ the full vector diffraction model presented in chapter 2 to numerically compute the intensity map of each part at the focal plane. To this purpose it is necessary to simulate the focusing of each transverse section individually, setting the integration domain coherently with the portion of the OAP selected by the considered section.

In what follows we investigate the generation of a 4-pulses train, meaning that the mask will consist of 4 different sections. In FIG. 3.2 a schematic representation of our idea is shown. The geometric center of the mask lays always on the optical axis of the incoming beam, which is the same axis where also the OAP center lays. At this stage we are neglecting the sections thickness since it is related only to the temporal characterization, which is later presented. The parameters of the simulations are fixed since the only variable is the integration domain, i.e. the sections area, and are listed in TAB. 3.1.

TABLE 3.1: Values of the parameters used in the simulations on the focusing of the different sections of the mask.

Parameter	Symbol	Value
Wavelength	λ	800 nm
Super-gaussian index	n	4
Constant amplitude	A_0	1
Initial beam extension	FWHM	40 mm
Polarization	δ	90°
Off-axis angle	θ_{OA}	25°
F-number	$f/\#$	5

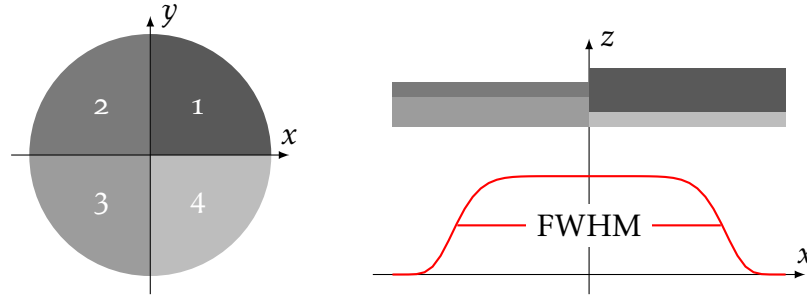


FIGURE 3.3: The first mask design considered. It is subdivided in quarters and its extension cover the entire transverse profile of the original beam.

In the next subsection a discussion on early dismissed designs is presented, with the intention of both underlining the versatility of the simulation model developed and displaying the necessary “flawed” steps in the development of a new, hopefully useful, technique.

3.2.1 EARLY DESIGNS

The first design considered consists of a circle subdivided in its 4 quarters as depicted in FIG. 3.3. The diameter of the circle is large enough to cover the entire transverse profile of the incoming beam and every sections evidently have the same area, thus yielding the same amount of initial energy.

The results of the 4 simulations are shown in FIG. 3.4. The intensity in

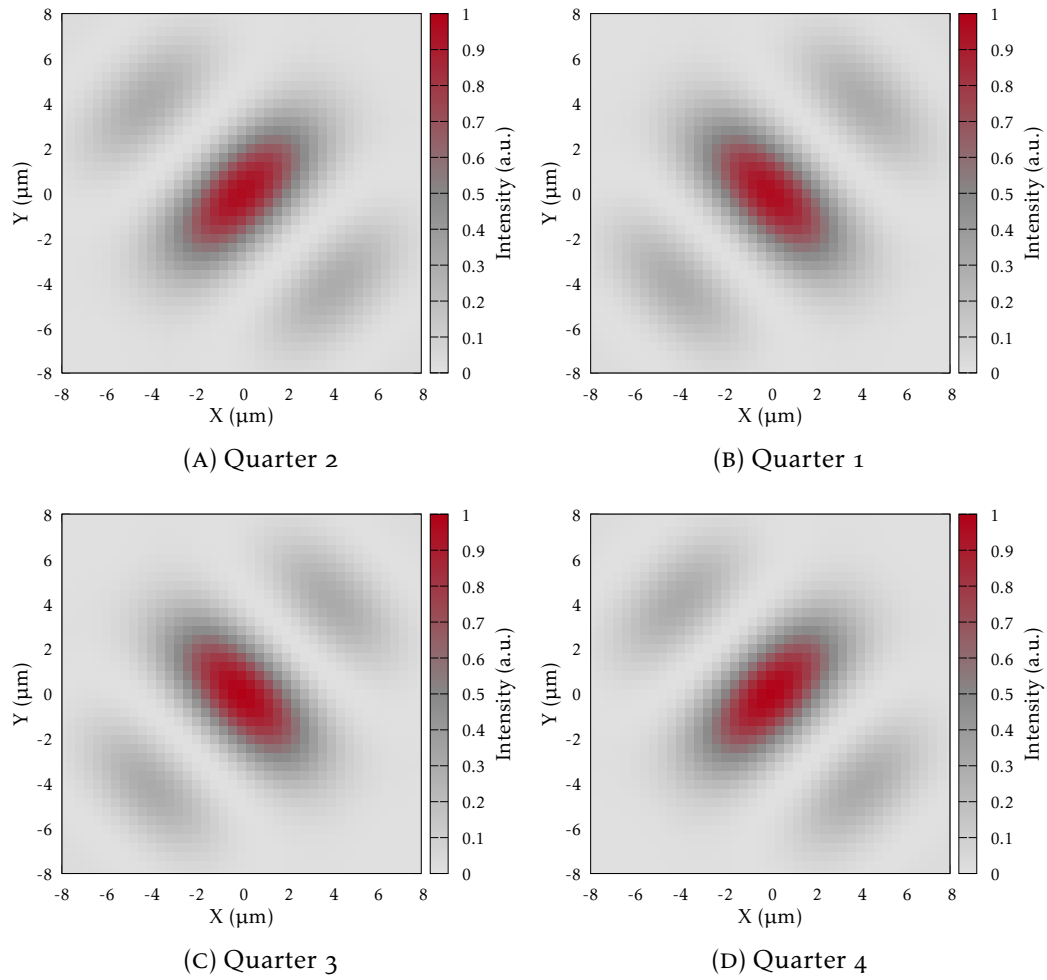


FIGURE 3.4: Intensity maps of the 4 pulses within the first mask design. The magnitude in every plot is normalized with the same peak intensity.

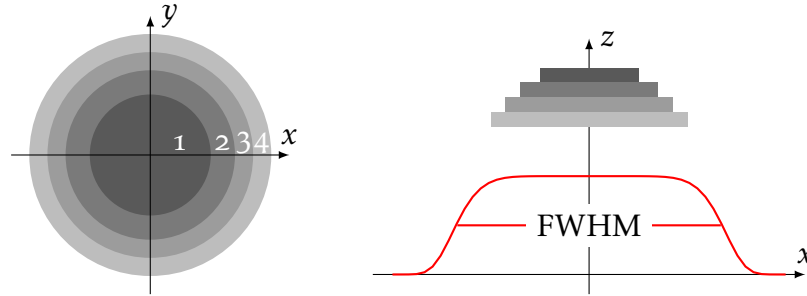


FIGURE 3.5: The second mask design investigated. In this case circular sections of the same area aim to respect the cylindrical symmetry of the incoming beam thus obtaining a better spot shape. The maximum diameter is set to $\text{FWHM}/2$ in order to grant the same energy for each section.

each plot is normalized to the same peak intensity value, found, as expected, at the center of the plane. The main realization from the intensity plots of each focused pulse is that the condition of same energy for every section corresponds actually to the same peak intensity delivered at focus. However the evident anisotropies between the spatial spots make this design not acceptable.

The first attempt made clear the importance of keeping a rotational symmetry, with respect to the incoming beam, in the geometry of the mask. Therefore the second design investigated consists of 4 concentric regions, as showed in FIG. 3.5: an inner circle and 3 outer rings. In order to respect the condition of same energy per section area, the radii of the circular sections are calculated as

$$r_i = \sqrt{i}r, \quad (3.3)$$

where $i = 1, 2, 3, 4$ refers to each circle and r is the radius of the inner one. For the same reason the total diameter of the mask in this case is set to be half the FWHM of the beam. In fact, with this assumption, all the sections correspond to the flat region of the transverse super-gaussian profile, ensuring an equal amount of energy for each pulse. The obvious energy loss due to the exclusion of the tails is not relevant at this stage since we are only interested in the spatial effect of such a design to the focused

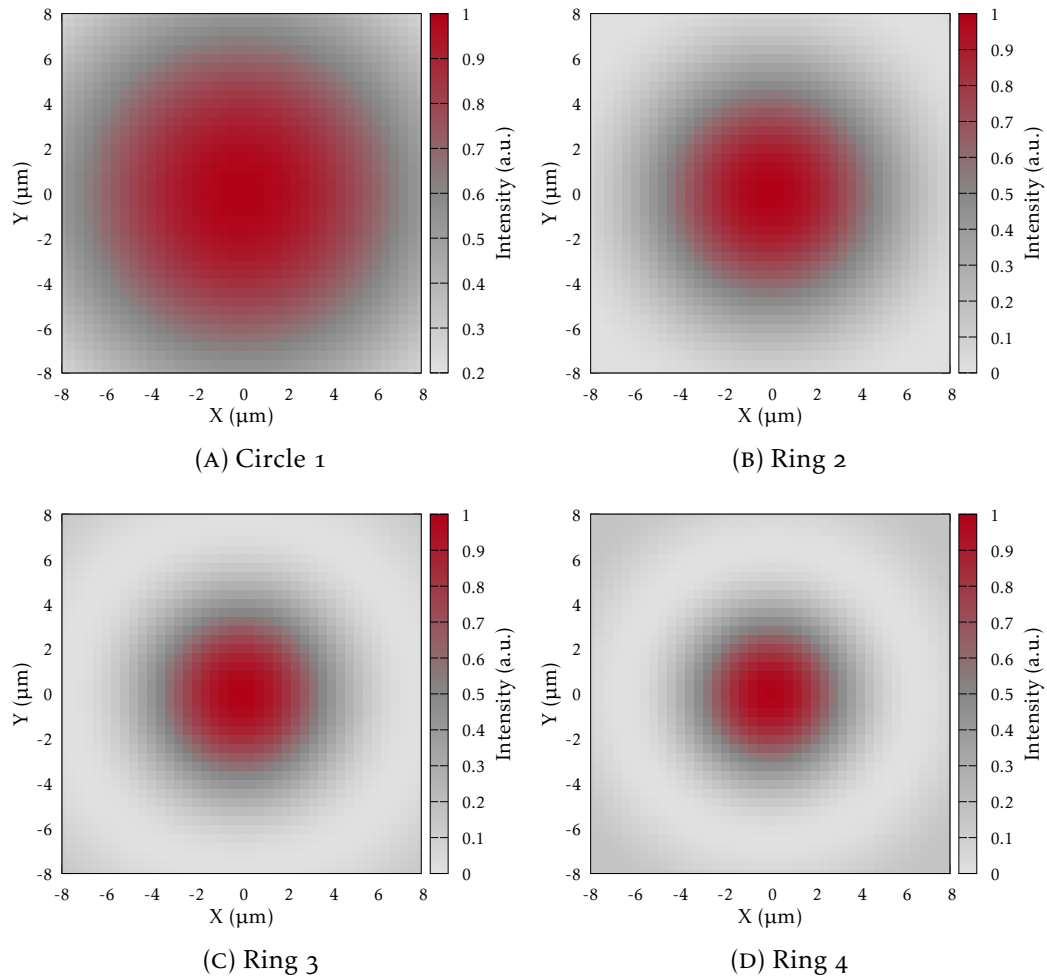


FIGURE 3.6: Intensity maps of the 4 pulses within the first mask design. The magnitude in every plot is normalized with the same peak intensity.

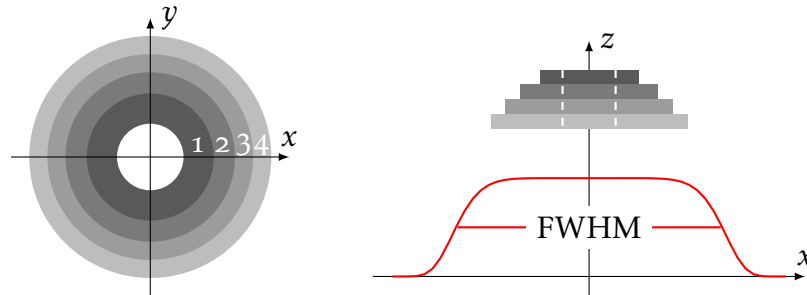


FIGURE 3.7: Final design of the delay mask. It retains the properties of the second design introducing though a hole in the middle in order to mitigate the difference between the focal spot sizes and allow the pick up of the ionizing pulse in the ReMPI scheme.

spot. In particular, recalling that $\text{FWHM} = 40 \text{ mm}$, r is set to be 5 mm .

FIG. 3.6 reports the results of this second set of simulations. The intensity maps, normalized by the peak intensity at center as before, exhibit the desired cylindrical symmetry and confirm the relation between peak intensity and same area per energy. However the plots highlight also an effect of “apparent” f-number, making the spot size not quite comparable. Due to the symmetry it is possible, for a better visualization, to plot the lineout of the X axis, as in FIG. 3.8(A). It is to be noticed that the inner circle 1 presents the bigger difference in spot size, while the ones corresponding to the outer rings are rather similar although diffraction effects seem to become more important.

3.2.2 FINAL DESIGN

As the final iteration of the design process, we modified the second design by introducing a hole in the middle. This solution has 2 reasons: it takes care of the inner circle issue and fulfills the requirement of the ReMPI scheme to obtain the ionizing pulse as part of the original one. In fact the part of the initial beam corresponding to the hole, hence not interacting with the mask, can be separately picked up, doubled in frequency and

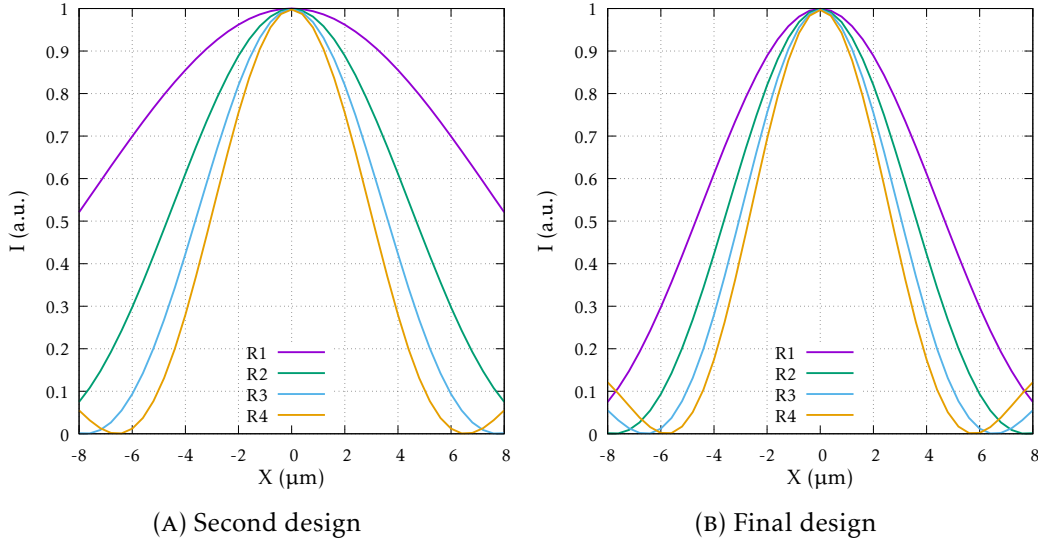


FIGURE 3.8: Intensity lineouts for the rotationally symmetric designs. The condition of same energy per area still grants the intensity peak to be equal for every subpulses. In the second design, the “full-body” one, the difference between the inner circle spot size and the others is quite evident making the final design, with a hole in the middle, more acceptable in terms of spot size difference and also for the ionizing pulse pick up.

reinserted in the main line, providing the ionization pulse. However this aspect is beyond this thesis to be discussed. This final design is depicted in FIG. 3.7. Besides the presence of the hole, all the previous consideration on the energy per area still hold in place. The dimensions of the rings are the same as before, with the addition of the outer ring 4 having an external radius of $r_4 = \sqrt{5}r$.

In this case we simply report the intensity lineout of the 4 subpulses in FIG. 3.8(B). As expected it summarizes all of the previous observations:

- pulse sections with an equal amount of energy per area provide the same peak intensity when focused;
- rotationally symmetric sections turn out to retain a symmetric (bell-shaped) spot size at the focal plane;

- ring-shaped sections have comparable spot size, despite stronger diffraction effects.

On a lesser positive note, it is worth noticing that the diffraction due to the ring geometry introduces a significant energy loss. The central spot of the focused pulses retains only a 10 to 20 % (depending on the radius) of the energy carried by the corresponding initial ring pulse. However the loss can be taken into account and experimentally compensated with a higher-energy initial pulse.

Further simulations, not reported in this thesis for conciseness, with higher f-number (which is usual in LWFA experiments) showed no difference in either energy loss or focal spot size variations. That is why the most attention has been devoted to the mask geometry, which is clearly the main responsible for the spatial characterization of each pulse of the train.

This preliminary analysis, made possible by the flexibility of the developed simulation model, displays the, otherwise difficult to grasp, relations between the transverse shape of the different sections of the delay mask and the spatial properties of the focal spot of the corresponding subpulses. It is important to notice that these results are strictly related to the imposed, relatively arbitrary, conditions; working in parallel with plasma simulation can underline which one of these properties is most important or which are the best conditions to match in terms of plasma wakefield in order to refine the mask.

3.3 TEMPORAL CHARACTERIZATION

As shown, the transverse structure of the mask and its sections are related mainly to the focal spot quality. The temporal aspects of the pulse train instead concern the thickness of them and the medium optical properties.

The main requirement for the pulse train in a MP-LWFA scheme is to have each pulse delayed from each other by a plasma period in order to resonantly excite the plasma wakefield. This, applied to the mask, means

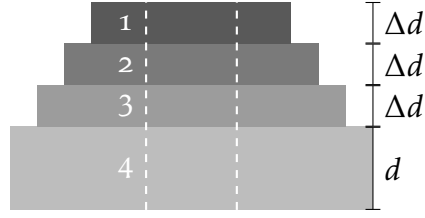


FIGURE 3.9: The optical path difference Δd , corresponding to the sections thickness, of a subpulse propagating in vacuum with respect to the one in the medium is responsible for the delay between each subpulse. This delay should match the plasma period for MP-LWFA purpose.

that a subpulse emerging from one section should be delayed of a plasma period with respect to the one emerging from the adjacent section. In other words, for a given thickness Δd , the difference in group velocities between a subpulse propagating in the medium and the adjacent one propagating in vacuum introduces a delay Δt given by

$$\Delta t = \Delta d \left(\frac{1}{v_g} - \frac{1}{c} \right) \quad (3.4)$$

that should, in fact, be made to match the plasma period.

In order to estimate the sections thickness it is necessary to recall the definitions from chapter 1 of plasma period and group velocity. The former can be readily deduced from the plasma frequency as

$$T_{pe} = \frac{2\pi}{\omega_{pe}} = \frac{2\pi}{\sqrt{\frac{n_e e^2}{m_e \epsilon_0}}}, \quad (3.5)$$

where n_e , e and m_e are the density, the electric charge and the mass of the electrons respectively and ϵ_0 the permittivity of free space. The group velocity of a pulse propagating through matter, as already retrieved in the context of linear dispersion, is written, specifying the wavelength dependence upon the refractive index of the medium, as

$$v_g = \frac{c}{n} \frac{1}{1 - \frac{\lambda}{n} \frac{dn}{d\lambda}}, \quad (3.6)$$

TABLE 3.2: Dispersion parameters for different types of glass at 800 nm wavelength.

Material	n	$\frac{dn}{d\lambda}$ (μm^{-1})	GVD ($\text{fs}^2 \text{mm}^{-1}$)	TOD ($\text{fs}^3 \text{mm}^{-1}$)
Fused Silica	1.453	-0.017	36.16	27.47
N-LakL21	1.633	-0.025	61.40	41.42
N-SF10	1.711	-0.050	156.52	102.52
N-BK7	1.511	-0.020	44.65	32.10

where c is the speed of light, n the refractive index of the material, λ the central wavelength of the pulse and $\frac{dn}{d\lambda}$ is the chromatic dispersion. The value of this last parameter (and also high order dispersion terms) is typically tabulated for any optical material depending on the central wavelength considered. For example in TAB. 3.2 different types of glass are listed with their optical parameters valid for a wavelength of 800 nm.

Finally, substituting in eq. (3.4) the expression for the group velocity and considering $\Delta t \equiv T_{pe}$, the difference of thickness between two adjacent sections can be written as

$$\Delta d = \frac{cT_{pe}}{n\left(1 - \frac{\lambda}{n} \frac{dn}{d\lambda}\right) - 1}. \quad (3.7)$$

From now on, it is necessary to relate to a realistic scenario, or at least consider a typical experimental setup in order to provide a deeper analysis. Only in this way it is possible to evaluate the order of magnitude of the phenomena involved and explore the actual feasibility of the delay mask.

Upon the plasma properties, the initial electron density is the only parameter needed to calculate the plasma period. In LWFA experiments, where the target of the laser pulse is usually a gas-jet, electron density is of the order of 10^{18}cm^{-3} . Hence considering $n_e = 1 \times 10^{18} \text{cm}^{-3}$ one gets $T_{pe} \simeq 111 \text{fs}$.

The choice of the material the mask is made of was obviously taken to be the least impactful on the pulse properties, mainly in terms of GVD. Hence,

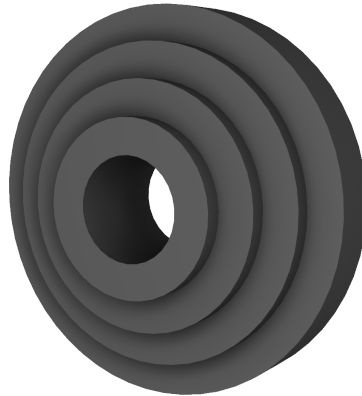


FIGURE 3.10: A 3D rendering of the delay mask.

from TAB. 3.2 it is clear the advantage of employing fused silica glass. So, considering an operational wavelength of 800 nm for the original laser pulse and using the dispersion parameters of fused silica, from eq. (3.7) one finally gets $\Delta d \simeq 71 \mu\text{m}$.

This thickness difference, analytically calculated, could seem difficult to obtain in reality, given its order of magnitude and the precision required by these kind of laser pulses. However, (after a preliminary check with a specialized company) it is possible with modern manufacturing technology to produce self standing fused silica slabs with a minimum thickness of 500 μm . This means, in regard to the design of the delay mask, that the biggest outer section (namely the ring 4 in FIG. 3.9) must have a thickness d of (at least) 500 μm but the other rings can be fused (or carved) on it. Since the delay between the pulses depends solely on the difference between sections thickness, the addition of a wide “base” is not an issue. However, the presence of a bigger quantity of material to be passed through by the laser pulse, can enhance the dispersion effects.

Once determined the actual thickness of each ring (reported in the second column of TAB. 3.3) and acknowledging the “unplanned” additional base, a deeper analysis is necessary to assess dispersive effects. Hence the propagation of the laser pulse through the different sections of the mask

TABLE 3.3: Duration of pulses in the train. Considering an initial pulse with a duration of 30 fs, it is reported the GVD-related time broadening of each pulse of the train emerging from the respective ring. The fourth column shows the duration broadening for an initial pulse with a $-1 \times 10^{27} \text{ s}^{-2}$ frequency chirp.

Ring	Thickness (μm)	FWHM (fs)	FWHM _c (fs)
1	713	38.5	35.6
2	642	37.2	34.6
3	571	36.0	33.7
4	500	34.8	32.8

was simulated via Miro [44], a powerful software for high-energy pulse amplification and propagation. In particular, in these simulations the quasi-1D numerical scheme was employed and nonlinear and dispersive (up to the second order) effects were taken into account. The idea is to carry 4 different simulation runs, one for each ring, where a single pulse pass through a fused silica plate of the appropriate thickness. As well as the temporal properties were neglected in the spatial characterization, these simulations concern ideally the temporal description of a “single” ray which can then be extended to the transverse profile of each ring.

The original pulse is defined by the usual wavelength of 800 nm, an energy of 1 J and a duration, expressed as FWHM of the Gaussian envelope, of 30 fs while the dispersion parameters of fused silica are listed in TAB. 3.2. The main result to consider, and the most relevant one, is the time broadening, due to both linear dispersion and GVD, that is the duration, still evaluated as the FWHM, of each subpulse after passing through the corresponding ring of the mask. The results are reported in the third column of TAB. 3.3. As it can be seen, the thinner section (ring 4) introduces a nearly-5 fs and furthermore a difference in duration between the subpulses emerging from the inner ring (1) and the outer one (4) of approximately 10% arises as a consequence of pulse propagation. Preliminary plasma

simulations show that this broadening is utterly acceptable in terms of wake excitation.

However, pulse propagation theory shows that it is also possible to mitigate the pulse duration broadening via the use of an initially chirped pulse. For instance, introducing a negative chirp of 10^{27} s^{-2} as an input parameter for the Miro simulations results in the durations reported in the fourth column of TAB. 3.3. Clearly this second set of results seem more suited for the experimental implementation but the main objective of this work is to stress out the different viable possibilities offered by the delay mask, deferring to further comprehensive plasma simulations the “burden” of selecting the most appropriate conditions for MP-LWFA.

The reported results already suggest a low impact of the nonlinear effects occurring in the pulse propagation. As a final check, though, on the acceptability of this model, the B -integral is retrieved from the Miro simulations. This quantity is defined as

$$B = \frac{2\pi}{\lambda} \int n_2 I(x) dx, \quad (3.8)$$

where $I(x)$ is the intensity along the beam axis of propagation x and n_2 is the nonlinear index. Recalling that $n_2 I$ is the nonlinear change in the refractive index, B -integral represents the total nonlinear phase shift accumulated by the beam through propagation into the medium. Therefore it serves as an indicator of the relevance of nonlinear effects in the system considered: values larger than the unit suggest such relevance which can manifest itself by means of self-focusing, destructive, phenomena. The Miro estimated B -integral for every run of simulations was of the order of 10^{-1} , thus confirming that the dimensions considered for this model can be safely tolerated in any practical situation.

CONCLUSIONS

The entire process of designing an optical component, including motivation, specifications, concept and modeling, has been presented in this thesis. A set of different tools and skills have been employed, taking all the necessary steps starting from the development of a thorough theoretical framework not yet presented, to our knowledge, in literature. Continuing with the development of an original code retaining the generality and flexibility of the theoretical model.

A deep analysis of a phenomenon regarding sub-cycle depolarization for laser beam focused by OAP has also been provided, validating and integrating experimental measurements of anomalous fields presented by other researchers. Future prospects are to include a better knowledge of the temporal dynamics.

And finally an intensive study on the characterization of the spatial and temporal profile of a pulse train generated by means of a delay mask has been carried, employing both our original simulation model and a third party software. As discussed, the proposed solution for pulse train generation based on a delay mask has some limitations concerning the focal spot size, but is simple and easy to implement experimentally and is foreseen as a possible option for preliminary tests on the resonant multi-pulse wakefield generation.

ACRONYMS

AFL	Apparent Focal Length
CPA	Chirped Pulse Amplification
CW	Continuous-Wave
FEL	Free Electron Laser
FWHM	Full Width at Half Maximum
GVD	Group Velocity Dispersion
LWFA	Laser WakeField Acceleration
MP-LWFA	Multi-Pulse Laser WakeField Acceleration
OAP	Off-Axis Parabola
ReMPI	Resonant Multi-Pulse Ionization injection
ROI	Region Of Interest
TNSA	Target Normal Sheath Acceleration

BIBLIOGRAPHY

- [1] T. TAJIMA and J. M. DAWSON. Laser Electron Accelerator. *Phys. Rev. Lett.* **43**(4), 267–270 (1979).
- [2] A. J. GONSALVES *et al.* Petawatt Laser Guiding and Electron Beam Acceleration to 8 GeV in a Laser-Heated Capillary Discharge Waveguide. *Phys. Rev. Lett.* **122**(8), 084801 (2019).
- [3] P. TOMASSINI *et al.* The Resonant Multi-Pulse Ionization Injection. *Phys. Plasmas* **24**, 103120 (2017).
- [4] L. LABATE, G. VANTAGGIATO, and L. A. GIZZI. Intra-cycle depolarization of ultraintense laser pulses focused by off-axis parabolic mirrors. *High Power Laser Science and Engineering* **6**, e32 (2018).
- [5] J. D. JACKSON. *Classical electrodynamics* (John Wiley & Sons, 1999).
- [6] J. A. STRATTON. *Electromagnetic Theory* (Wiley, 2007).
- [7] M. BORN and E. WOLF. *Principles of Optics: Electromagnetic Theory of Propagation, Interference and Diffraction of Light* (Elsevier Science, 2013).
- [8] D. J. RICHARDSON, J. NILSSON, and W. A. CLARKSON. High power fiber lasers: current status and future perspectives. *JOSA B* **27**(11), B63–B92 (2010).
- [9] J.-C. DIELS and W. RUDOLPH. *Ultrashort laser pulse phenomena* (Academic press, 2006).
- [10] C. RULLIÈRE. *Femtosecond laser pulses* (Springer, 2005).

- [11] T. H. MAIMAN. Stimulated optical radiation in ruby. *Nature* **187**, 493–494 (1960).
- [12] F. J. MCCLUNG and R. W. HELLWARTH. Giant optical pulsations from ruby. *J. Appl. Phys.* **33**(3), 828–829 (1962).
- [13] A. H. HAUS. Mode-locking of lasers. *IEEE J. Sel. Top. Quantum Electron* **6**(6), 1173–1185 (2000).
- [14] G. MOUROU, T. TAJIMA, and S. BULANOV. Optics in the relativistic regime. *Rev. Mod. Phys.* **78**(2), 309–371 (2006).
- [15] D. STRICKLAND and G. MOUROU. Compression of amplified chirped optical pulses. *Opt. Commun.* **55**(6), 447–449 (1985).
- [16] F. CHEN. *Introduction to Plasma Physics and Controlled Fusion* (Springer, 1984).
- [17] A. MACCHI. *A superintense laser-plasma interaction theory primer* (Springer, 2013).
- [18] J. E. HOWARD. Imaging properties of off-axis parabolic mirrors. *Appl. Opt.* **86**, 2714–2722 (1979).
- [19] C. J. R. SHEPPARD, A. CHOUDHURY, and J. GANNAWAY. Electromagnetic field near the focus of wide-angular lens and mirror systems. *IEEE J. Micr. Optics Acoust.* **1**, 129–132 (1977).
- [20] J. A. STRATTON and L. J. CHU. Diffraction theory of electromagnetic waves. *Phys. Rev.* **56**(1), 99–107 (1939).
- [21] P. ARGUJIO, M. S. SCHOLL, and G. PAEZ. Diffraction patterns formed by an off-axis paraboloid surface. *Appl. Opt.* **40**, 2909–2916 (2001).
- [22] P. VARGA and P. TÖRÖK. Focusing of electromagnetic waves by paraboloid mirrors. I. Theory. *J. Opt. Soc. Am. A* **17**(11), 2081–2089 (2000).
- [23] P. VARGA and P. TÖRÖK. Focusing of electromagnetic waves by paraboloid mirrors. II. Numerical results. *J. Opt. Soc. Am. A* **17**(11), 2090–2095 (2000).

- [24] M. KEMPE and W. RUDOLPH. Femtosecond pulses in the focal region of lenses. *Phys. Rev. A* **48**, 4721–4729 (1993).
- [25] T. JEONG *et al.* Spatio-temporal modification of femtosecond focal spot under tight focusing condition. *Opt. Express* **23**, 11641–11656 (2015).
- [26] A. COUAIRON *et al.* Propagation equation for tight-focusing by a parabolic mirror. *Opt. Express* **23**, 31240–31252 (2015).
- [27] J. PEATROSS, M. BERRONDO, D. SMITH, and M. WARE. Vector fields in a tight laser focus: comparison of models. *Opt. Express* **25**(13), 13990–14007 (2017).
- [28] J. BERNSTEN, T. O. ESPELID, and A. GENZ. An adaptive algorithm for the approximate calculation of numerical integrals. *ACM Trans. Math. Soft.* **17**, 437–451 (1991).
- [29] L. LABATE, P. FERRARA, L. FULGENTINI, and L. A. GIZZI. Effects of small misalignments on the intensity and Strehl ratio for a laser beam focused by an off-axis parabola. *Appl. Opt.* **55**(23), 6506–6515 (2016).
- [30] K. SHIBATA, M. TAKAI, M. UEMOTO, and S. WATANABE. Intrinsic formation of electromagnetic divergence and rotation by parabolic focusing. *Phys. Rev. A* **92**(5), 053806 (2015).
- [31] M. TAKAI, K. SHIBATA, M. UEMOTO, and S. WATANABE. Spatial polarization variation in terahertz electromagnetic wave focused by off-axis parabolic mirror. *Appl. Phys. Express* **9**(5), 052206 (2016).
- [32] K. SHIBATA, M. UEMOTO, M. TAKAI, and S. WATANABE. Detailed study of transient anomalous electric field vector focused by parabolic mirror. *J. Opt.* **19**, 035603 (2017).
- [33] J. A. MURPHY. Distortion of a simple gaussian beam on reflection from off-axis ellipsoidal mirrors. *Int. J. Infrared Millimeter Waves* **8**, 1165–1187 (1987).

- [34] S. M. HOOKER *et al.* Multi-Pulse Laser Wakefield Acceleration: A New Route to Efficient, High-Repetition-Rate Plasma Accelerators and High Flux Radiation Sources. *J. Phys. B* **47**, 234003 (2014).
- [35] D. UMSTADTER, E. ESAREY, and J. KIM. Nonlinear plasma waves resonantly driven by optimised laser pulse trains. *Phys. Rev. Lett.* **72**(8), 1224–1227 (1994).
- [36] D. UMSTADTER, J. KIM, E. ESAREY, E. DODD, and T. NEUBERT. Resonantly laser-driven plasma waves for electron acceleration. *Phys. Rev. E* **51**(5), 3484–3497 (1995).
- [37] R. J. TEMKIN. Excitation of an atom by a train of short pulses. *J. Opt. Soc. Am. B* **10**, 830–839 (1993).
- [38] I. P. CHRISTOV, M. M. MURNANE, and H. C. KAPTEYN. High-harmonic generation of attosecond pulses in the ‘single-cycle’ regime. *Phys. Rev. Lett.* **78**, 1251–1254 (1997).
- [39] C. W. SIDERS, J. L. W. SIDERS, A. J. TAYLOR, S. G. PARK, and A. M. WEINER. Efficient high-energy pulse-train generation using a 2^n -pulse Michelson interferometer. *Appl. Opt.* **37**(22), 5302–5305 (1998).
- [40] B. DROMEY *et al.* Generation of a train of ultrashort pulses from a compact birefringent crystal array. *Appl. Opt.* **46**(22), 5142–5146 (2007).
- [41] R. J. SHALLOO *et al.* Generation of laser pulse trains for tests of multi-pulse laser wakefield acceleration. *NIM A* **829**, 383–385 (2016).
- [42] T. ROBINSON *et al.* Simple technique for generating trains of ultrashort pulses. *Appl. Opt.* **32**(15), 2203–2205 (2007).
- [43] J. COWLEY *et al.* Excitation and Control of Plasma Wakefields by Multiple Laser Pulses. *Phys. Rev. Lett.* **119**, 044802 (2017).
- [44] O. MORICE. Miro: Complete modeling and software for pulse amplification and propagation in high-power laser systems. *Opt. Eng.* **42**(6), 1530–1541 (2003).